Opposite page:

Scanning electron micrograph of a 100 nm-period grid, exposed in PMMA on top of an antireflection coating, and transferred into Si by reactive ion etching.

Courtesy of J.M. Carter, R.C. Fleming, T.A. Savas, M.E. Walsh, and T.B. O'Reilly (M.L. Schattenburg and H.I. Smith)

Sponsor:
DARPA and U.S. Army Research Office

Submicron and Nanometer Structures

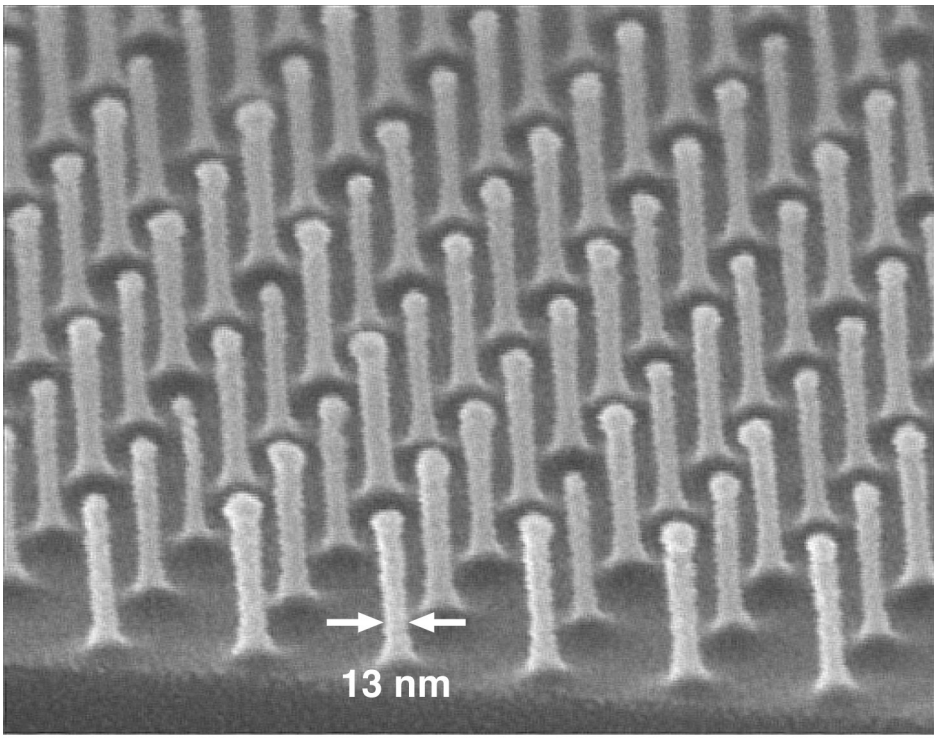

100nm-period posts in Si

Submicron and Nanometer Structures

- *Scanning-Electron-Beam Lithography*
- *Spatial-Phase-Locked Electron-Beam Lithograpy*
- *Zone-Plate-Array Lithography (ZPAL): The System*
- *Interference Lithography for Patterning Variable-Period Gratings*
- *Zone-Plate-Array Lithography (ZPAL): Lithographic Performance*
- *X-Ray Nanolithography*
- *Nanometer-level Feedback-Stabilized Interferometric Aligning and Gapping in an X-Ray Lithographic System*
- *Adaptive-Membrane-Mask Technology*
- *Interference Lithography*
- *The MIT Nanoruler: A Tool for Patterning Nano-Accurate Gratings*
- *Templated Self-Assembly*
- *Block Copolymer Lithography*
- *Precision Fabrication Techniques for Microphotonic Devices*
- *Nanopattern-Assisted Growth of Organic Materials for Device Applications*
- *Strain-Tunable Photonic Band Gap Microcavity Waveguides at 1.55 μm*
- *Nanopelleting of Carbon Nanotubes*
- *Nanofabricated Metal Transmission Gratings*
- *Nanofabricated Reflection Gratings*
- *Transmission Gratings for X-Ray and Atom-Beam Spectroscopy and Interferometry*
- *X-Ray Foil Optics Shaping Technology*
- *Nano-Accurate Assembly Technology for X-Ray Foil Optics*
- *Functional 3D Nanostructures Achieved via Folding of 2D Membranes*
- *Integration of Nanowires Embedded in Anodic Alumina Templates with a Large Silicon Substrate*

Scanning-Electron-Beam Lithography

Personnel

J.T. Hastings, M.K. Mondol, and F. Zhang (H.I. Smith)

Sponsorship

NSF, DARPA, and U.S. Army Research Office

Figure 1 is a photograph of the Scanning-Electron-Beam Lithography system (VS-26) located in the Scanning-Electron-Beam Lithography (SEBL) facility, Room 38-165. This instrument was put together at MIT from two systems (VS-2A and VS-6) obtained as gifts from IBM in the mid 1990's. It has a minimum beam diameter of about 12 nm and is capable of creating large-area patterns composed of multiple stitched fields. Conversion software has been developed which allows a CAD data file to be fractured and translated prior to exposure by the electron-beam tool. Substrates up to 20 cm diameter can be exposed at linewidths down to 30 nm. In order to write concentric circular patterns, such as Freznel zone plates, software was developed to generate arbitrary arcs of an annulus with user-specified start and finish radii and angles.

The SEBL facility also houses a Raith Turnkey 150 system as shown in Figure 2. Its electron-optical column is essentially identical to that of a Gemini SEM, and provides a beam diameter as fine as 5 nm. Linewidths of 17 nm have been written with the system, as illustrated in Figure 3.

The goals of the SEBL facility are to: (1) provide the MIT research community with an in-house SEBL capability for writing directly on experimental device substrates; (2) advance the state-of-the-art in SEBL, particularly with regards to pattern placement accuracy and long-range spatial-phase coherence; and (3) pattern photomasks and X-ray nanolithography masks for in-house use.

The VS-26 and Raith 150 are heavily used in a variety of projects, both mask making and direct write. These have included: 3-D, 2-D, and 1-D photonic bandgap structures; optical-communication filters; arrays of Fresnel zone plates; electrical contacts to bismuth nanowires; high-density magnetic nanodots and rings for information storage; distributed-feedback lasers; sub-100 nm electronic devices; double-gate sub-100nm MOSFETs; diffractive optical elements; and magnetic random access memory devices. Masks have been made for X-ray nanolithography and conformable-contact photolithography.

The Raith 150 is used in a program to develop spatial-phase-locked e-beam lithography. The objectives of this program are (1) to achieve sub-1 nm pattern-placement accuracy, and (2) to reduce the cost and complexity of SEBL. In a conventional SEBL system costing several million dollars, pattern placement accuracy is typically much worse than 10 nm.

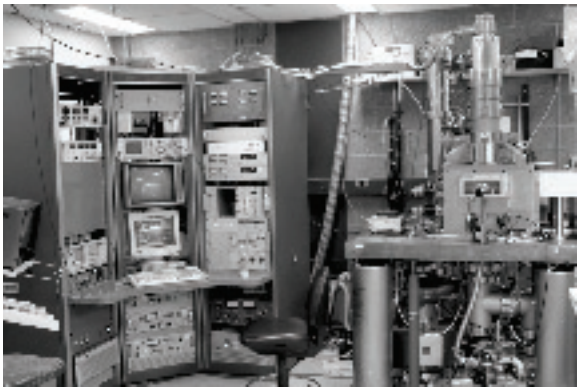

Fig. 1: Photograph of the VS-26 scanning-electron-beam lithography system.

continued

continued

Fig. 2: The Raith-150 electron-beam lithography system. This tool provides sub-20-nm patterning resolution, and pattern-placement accuracy ~ 1nm via spatial phase locking. The operator is graduate student J. Todd Hastings.

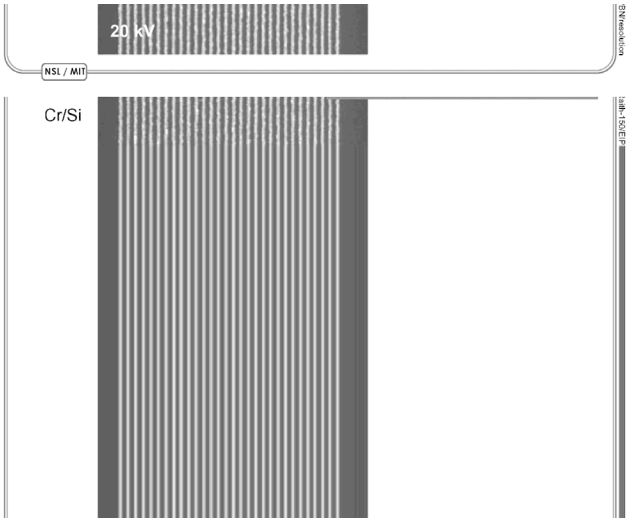

Fig. 3: Scanning electron micrograph illustrating the resolution of the Raith 150 SEBL system.

Spatial-Phase-Locked Electron-Beam Lithography

Personnel

C. Caramana, Dr. J. Goodberlet, J.T. Hastings, M.K. Mondol, and F. Zhang (H. I. Smith)

Sponsorship

DARPA and U.S. Army Research Office

Our research in Spatial-Phase-Locked Electron-Beam Lithography (SPLEBL) is aimed at reducing pattern-placement errors in electron-beam-lithography systems to the nanometer level. Such high precision is essential for a variety of future lithographic applications. SPLEBL is currently the only approach capable of achieving such accuracy. As shown in Figure 4, SPLEBL uses a periodic signal, derived from the interaction of the scanning e-beam with a fiducial grid on the substrate, to continuously track the position of the beam while patterns are being written. Any deviation of the beam from its intended location on the substrate is sensed, and corrections are fed back to the beam-control electronics to cancel errors in the beam's position. In this manner, the locations of patterns are directly registered to the fiducial grid on the substrate.

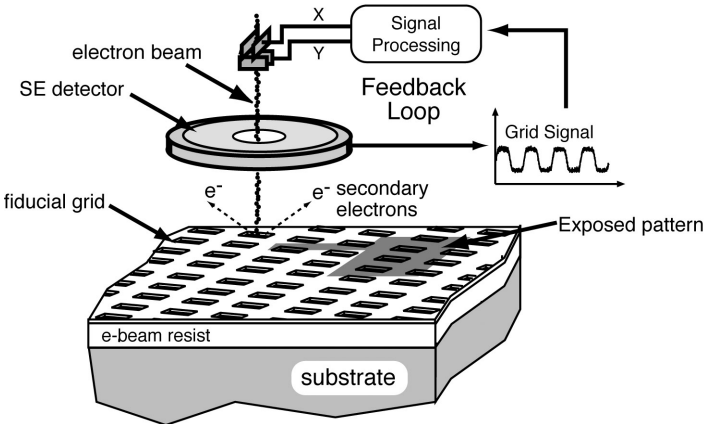

Fig. 4: Schematic of the global-fiducial-grid mode of spatial-phase-locked electron-beam lithography. The periodic signal detected from the fiducial grid is used to measure placement error, and feed a correction signal back to the beam deflection system.

We have implemented two modes of spatial-phase locking on a Raith 150 scanning e-beam lithography system. The Raith 150 is an inexpensive system that provides high resolution (sub-20-nm) patterning. It has little shielding from environmental disturbances and has a number of shortcomings with respect to pattern fidelity. Because the system can only reliably deflect the e-beam over a small area (~100 x 100 mm), patterns must be built up by stitching together an array of these fields. The best field-to-field stitching errors observed without spatial-phase locking have a standard deviation of ~8 nm.

continued

In the first mode of spatial-phase locking, the fiducial grid is segmented into small areas of the substrate that will not be patterned. Before exposing each stitched field, the electron beam scans over these areas and detects the spatial-phase of the grid. As a result, the field's shift, scaling, and rotation can be corrected before writing the pattern. This technique achieved field stitching errors with a standard deviation of 2.6 nm and has been used to expose 225-nm-period Bragg-grating filters in silicon-on-insulator waveguides.

To achieve maximum pattern-placement accuracy, it is desirable to constantly correct the beam position during exposure; to do so requires that the grid cover the entire substrate, but not perturb the electron-beam. Toward this end, we place a thin (<10 nm) metallic fiducial grid on top of PMMA e-beam resist. This grid produces a secondary-electron signal, while the primary electron-beam passes easily through to expose the resist below. Because the grid is conductive, it opens the possibility of obtaining higher signal-to-noise ratios through voltage contrast.

In order to implement the continuous-feedback mode, it was necessary to add raster-scan capability to the Raith 150. We added the required hardware and software to switch the beam on and off at desired times as the system raster-scans the beam across the field. In addition, we implemented hardware and software to measure the residual field distortion relative to the fiducial grid and to apply 3rd order corrections during the raster-scan exposures.

To provide continuous feedback control for beam positioning, we developed a phase-locking algorithm. The e-beam is scanned at an angle to the fiducial grid axes. This produces a signal with two fundamental frequency components whose phases are used to calculate the x- and y- beam-placement errors. To implement this algorithm, we added analog-to-digital conversion for the secondary electron signal, digital-signal processing with custom software for correction calculations, and digital-to-analog conversion for the x- and y- correction signals.

To evaluate the effectiveness of this algorithm, we exposed test patterns with a 10 keV electron beam using an 8-nm thick, 250-nm period, Al fiducial grid. Figure 5 shows stitching measurements of the resulting pattern with standard deviations at or below 1.3 nm. Locking to the fiducial grid ensures a comparable level of global pattern-placement accuracy. These experiments were conducted with patterns that do not require beam-current modulation to continuously track the grid. Developing appropriate current-modulating electron optics remains a high priority to enable patterning of arbitrary patterns. Another high priority for future research is to develop a means of putting down the fiducial grid that does require multi-step lithography.

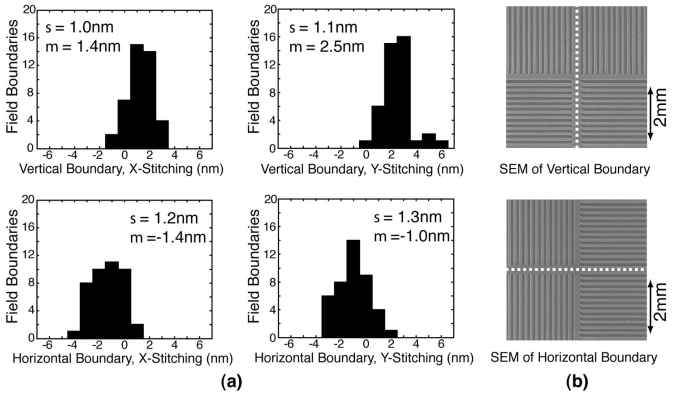

Fig. 5: (a) Histograms showing x- and y-stitching measurements at all 84 field boundaries of 49 stitched fields. Spatial-phase locking has reduced the standard deviation of the stitching errors to below 1.3 nm. (b) Sample 200-nm period stitched grating patterns. The dashed line indicates the field boundary.

Zone-Plate-Array Lithography (ZPAL): The System

Personnel
D. Gil, R. Menon, and A. Patel (H.I. Smith)

Sponsorship
DARPA and Army Research Office

In semiconductor lithography, glass masks are illuminated with deep UV laser light, and their image is reduced through a lens onto the substrate to define circuitry. As feature sizes are pushed towards 100 nm and smaller, lithography systems and masks are becoming increasingly complex and costly (~$1 million per mask set). In addition, the delay in obtaining a mask set, with complex optical-proximity correction and phase-shifting features can be months. This presents a huge hurdle to continuing progress in semiconductor technology.

At the MIT NanoStructures Laboratory, we are pursuing a radically new schem, which requires no mask called Zone-Plate-Array Lithography (ZPAL), made possible by inexpensive, high-speed computation and micromechanics. ZPAL replaces the "printing press" of traditional lithography with a technology more akin to that of a laser printer. Although it will not have the throughput of an optical stepper, ZPAL is ideal for prototyping and also for semiconductor products requiring only a few wafers, e.g., application-specific IC's.

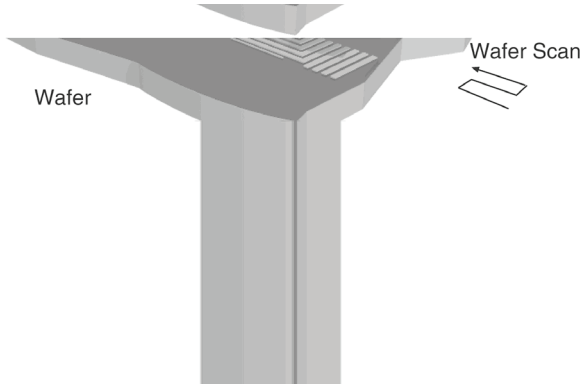

Fig. 6: Schematic of Zone-Plate-Array Lithography (ZPAL). An array of Fresnel zone plates focuses radiation beamlets onto a substrate. The individual beamlets are turned on and off by upstream micromechanics as the substrate is scanned under the array. In this way, patterns of arbitrary geometry can be created in a dot-matrix fashion. The minimum linewidth is equal to the minimum width of the outermost zone of the zone plates.

Instead of a single, massive lens, an array of hundreds or thousands of microfabricated Fresnel-zone-plate lenses is used, each focusing a beam of light onto the substrate. A computer-controlled array of micromechanical mirrors turns the light to each lens on or off as the stage is scanned under the array, thereby printing the desired pattern in a dot-matrix fashion. No mask is required, enabling designers to rapidly change circuit designs. A schematic of ZPAL is shown in Figure 6.

ZPAL leverages advances in nanofabrication, micromechanics, laser-controlled stages, and high-speed, low-cost computation to create a new form of lithography.

Recent research efforts have primarily concentrated on developing planar processes for fabrication of zone-plate arrays, proving the lithographic capabilities of zone plates, developing robust system-simulation tools and building a fast data-delivery system.

Fabrication of Phase-Zone-Plate Arrays

Phase-zone-plate arrays are fabricated using a process consisting of electron-beam lithography and self-aligned electrochemical etching. We use the negative e-beam resist HSQ (hydrogen silsesquioxane, by Dow Corning). HSQ's extraordinarily high resolution (~10nm) and its glass-like properties make it an optimal choice for fabricating diffractive-optical elements that operate in the UV and DUV regimes (See Figure 7). HSQ has an index of refraction very close to that of fused silica, and negligible absorption down to 157nm. The resist is first spun to the thickness corresponding to the desired phase step for the zone plate, patterned with e-beam lithography, and then the unexposed regions are developed away. It is also necessary to prevent the light from transmitting through those areas on the substrate not occupied by the zone plate. This is achieved by evaporating metal (chrome in this case) onto the substrate. Since the metal within the zones of the zone plate is electrically isolated from the metal outside,

continued

continued

the metal within the zone plate can be removed by an electrochemical etching process (Fulton/Dolan Process).

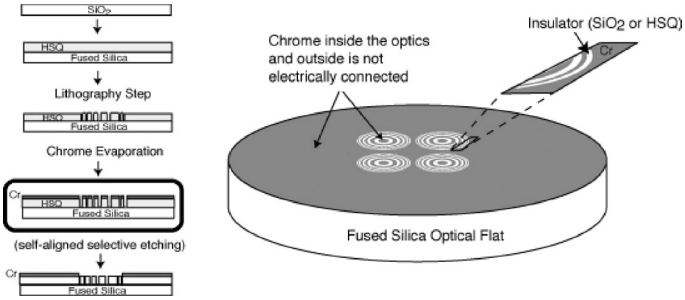

Fig. 7: Left: Typical sequence of the self-aligned process requiring a single-lithography step. Starting with a transparent blank material, HSQ is spun on it. The thickness of the HSQ is chosen to provide the appropriate phase step for the zone plate. After patterning the elements in HSQ, the absorber metal is evaporated. Right: Detail of the process after the absorber has been evaporated. Note that the absorber (chrome in this case) inside the zone plate and outside is not electrically connected. The lack of electrical connectivity will allow for the absorber within the diffractive elements to be removed by means of a wet-etch Fulton/Dolan technique.

Zone-plate arrays can be manufactured in a highly reliable manner. We have fabricated zone plates that perform very close to their theoretical limit (as shown in another section), and have manufactured arrays containing over 1,000 zone plates (See Figure 8). We believe much larger arrays, of ~1M zone plates, are possible.

System Simulation Tools

We have developed simulation tools to design zone plates as well as other diffractive focusing elements and to study the effect of various system parameters on the lithographic performance of ZPAL.

The simulation begins with modeling the diffraction of light by a zone plate using the finite-difference time-domain method. Calculated fields are further propagated to the focal plane of the zone plate using a vector

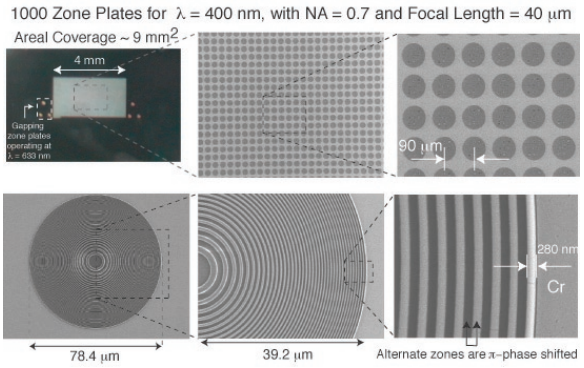

Fig. 8: Large zone plate arrays can be readily fabricated with our novel process that requires a single lithography exposure and no etching, even for the case of phase zone plates. Top-left: Optical micrograph showing an array containing over 1,000 zone plates with an aerial coverage of 9 mm². Bottom-right: Detail of the outermost zones. The duty-cycle is very close to 50%, and the phase shift between alternate zones was controlled to about 1%.

plane-wave spectrum method. Since this is a full-vector model of electromagnetic theory, it gives extremely accurate predictions about the spatial structure of the Point-Spread Function (PSF). This is illustrated in Figure 9, where the PSF of the zone plate was experimentally determined by exposing single spots at a large number of doses in photoresist. The photoresist, being highly nonlinear, acts as a sampler to obtain points on the PSF. The excellent agreement between the model and experiment attests to the model's accuracy as well as the reliable fabrication of the zone plates.

continued

continued

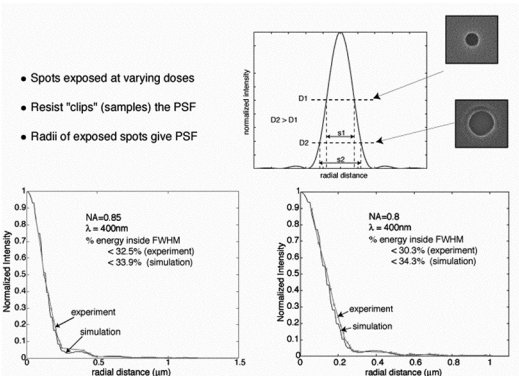

Fig. 9: Top: Experimental process for quantifying the PSF. Spots of several exposure times were patterned in photoresist, which acts as a sampler of the PSF. The radii of the exposed spots can be assembled to form the PSF. Bottom: PSFs for zone plates of NA=0.85 (left) and NA=0.8(right) were determined experimentally using the simulation tools. The results show excellent agreement.

Since ZPAL results in an incoherent addition of spots in photoresist, by convolving the PSF with a desired pattern, we can simulate exposed patterns. This is important to understand various component-tolerances in the system.

Micromechanics & Data Delivery System

We have switched from the previously reported method of multiplexing the light for ZPAL, the Texas Instruments DMD™ micromirror array, to the Silicon Light Machines Grating Light Valve™ (GLV™) linear array. Although the GLV™ has a smaller number of pixels (1,088) compared to the DMD™ micromirror array (~1 million or more), the higher speed of operation of the GLV™ (20ns rise time as opposed to 20 ms for the DMD™), the fact that gray-scaling is built in, and its diffractive mode of operation (making it compatible with shorter wavelengths, possibly even down to 157nm) made it a superior choice for ZPAL.

The GLV™ is a micromechanical phase grating consisting of parallel rows of reflective Al ribbons. Alternate rows of ribbons can be pulled down electrostatically in a controlled manner to create diffraction effects on incident light. When no force is applied, all the ribbons lie in the same plane. If illuminated, incident light will be reflected from their surfaces at the same angle at which it is incident. When alternate ribbons are pulled down, a grating structure is created. In this state diffraction will produce light at an angle different from that of the incident light. By alternating between these two states (i.e. from flat ribbons to a grating structure), the GLV™ can switch light ON and OFF. Furthermore, by tuning the applied electrostatic force, the depth to which the ribbons are pulled down can be controlled, impacting the amount of light diffracted into the first order. Grayscaling of the incident light can be achieved in this manner. Each of the 1088 pixels present in the linear array can accept 8-bits of grayscaling (256 levels). Since the motion involved in switching the pixels of the GLV™ is small (one-quarter wavelength), the GLV™ is capable of very high switching speeds, with a rise time from the ON to the OFF position of only 20ns. One pixel of the linear array is depicted schematically in Figure 10, along with the intended implementation in ZPAL.

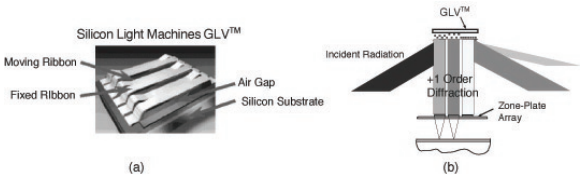

Fig. 10: Schematics of the Silicon Light Machines Grating Light Valve (GLV) device. (a): Fixed and electrostatically-deflected moving ribbons create a variable-height grating. (b): Incident light will be diffracted from the grating at a known angle, with varying intensity depending on the height of the grating. Each pixel, a small patch of the grating, diffracts onto a single zone plate, thus turning on and off (or grayscaling) each pixel written onto the substrate in ZPAL.

continued

continued

We have built a custom system to deliver the pattern data from the ZPAL control computer to the 1,088 pixels of the GLV™ array at very high speeds. Data is first transferred from the computer through the PCI bus to a National Instruments digital I/O board (Model#: 6601). The data is then sent from the I/O board to the GLV™ through a custom-made Printed Circuit Board (PCB) which performs the data routing and interpretation as required by the GLV™ electronics. The I/O board, equipped with an 80 Mhz clock to enable clocking the data at very high speeds, has the capability of both reading data from the control computer and sending data to the GLV™ simultaneously. In practice, two I/O boards are used in parallel to achieve high data rates. All the software was written in LabView on a Dell windows workstation.

In order to test the data delivery system, we have built an experimental setup as shown in Figure 11(a). Light from a Helium-Neon laser is collimated and directed onto the GLV™. A lens is used to focus the 1st order diffracted beam onto a detector. We send data to the GLV™ and measure the modulation of the light on the detector. Figure 11(b) shows the detector signal as a function of time when the GLV™ was driven with "ON-OFF" data at a frequency of 7.5 kHz (the specification required for our prototype system), corresponding to an average data transfer rate of 130 Mbits/s. The vertical axis is the detector voltage, but it was not calibrated and hence, is not labeled in the figure.

Since the GLV™ is capable of operating at much higher frequencies (~500 kHz), we tested our system to determine the limits of the data delivery architecture, even though our requirements had been successfully met. Figure 11(c) shows the GLV™ operating at a frequency of 66.67 kHz, corresponding to a data transfer rate of about 1Gbit/s. At present, we were limited by the response time of our detector, but data from our logic analyzer indicates that we can successfully send rates in excess of 100 kHz with our current

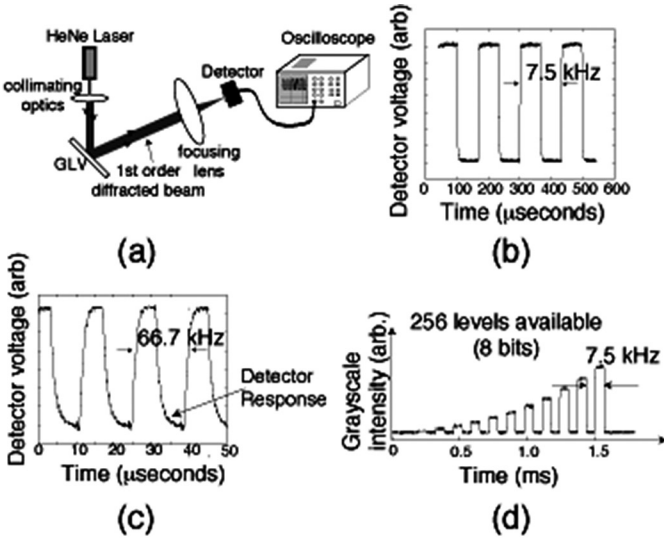

Fig. 11(a): Schematic of the experimental setup for testing the data delivery system for ZPAL. (b) The GLV operating at 7.5 kHz, the required speed for our prototype system. (c) The GLV operating at 66.67 kHz, corresponding to a 1Gbit/sec data rate. (d) Grayscaling at 7.5 kHz

implementation. Since dose control is an important requirement for good lithographic performance, the ability to grayscale is paramount in any multiplexing device to be employed in a ZPAL system. The GLV™ offers 8-bits of grayscaling (256 levels), 3 bits more than what is needed for our writing strategy, which requires 5-bits. As shown in Figure 11(d), our data-delivery system is capable of achieving all 8-bits of grayscaling without sacrificing switching speed.

Interference Lithography for Patterning Variable-Period Gratings

Personnel
C. Chen, C.-H. Chang, C. Joo, P. Konkola, J. Montoya, and R. Heilmann (M.L. Schattenburg)

Sponsorship
NASA

Scanning-Beam-Interference Lithography (SBIL) patterns large-area, linear, low-phase-distortion gratings with a pair of small diameter (millimeter size) phase-locked laser beams. We are developing a prototype system that generalizes the concept of phase-locked scanning beams for patterning continuously varying (chirped or quasi-periodic) patterns. These structures can subsequently be used to fabricate chirped X-ray reflection gratings for astronomical imaging applications, chirped fiber Bragg gratings for time-delay or spectral filtering applications, and/or diffractive optical elements.

Figure 12 shows the experimental diagram of the Variable-Period Scanning-Beam Interference-Lithography (VP-SBIL) system. For controlling the grating period and orientation, the system employs dual-axis picomotor-driven gimbal mirrors to produce symmetric deflections of a pair of interfering beams around the optical axis without translation. Two objective plano-convex lenses (f# = 4.25, 2.12) are used in a 4-f optical configuration. Such a lens system allows the conjugate points of beam deflection (on mirrors) to overlap at the focal plane of the second objective lens. The spot size of image overlap is reduced to half the beam diameter as the ratio of focal lengths f_2/f_1=0.5. This relaxes the maximum period variation ($\Delta\Lambda$) constraint over the image diameter (D) that requires $\Delta\Lambda/\Lambda << \Lambda/D$ where Λ is the grating period.

To attain phase stability during grating patterning, homodyne fringe locking is adopted using an imaging detector, analog fringe-locker and a piezo-actuated mirror in closed-loop. In the present experimental configuration, two-axis beam rotation can generate any fringe orientation. However, variation in grating period (~1000 to 2 μm) is limited by the range of deflection produced by the gimbal mirrors (± 10°) and by the numerical aperture (NA) of the lens system. Using position-sensitive detectors with an appropriate imaging and Fourier lens configuration, closed-loop beam steering is implemented to vary the grating period and orientation in a predetermined fashion. Typical requirements for x-ray reflection grating fabrication are Λ_{ave}~ 2 μm and chirp factor $\Delta\Lambda/\Lambda$ ~ 5%.

Figure 13 shows two grating images of period 2.0 μm and 4.0 μm obtained on a static substrate by changing the angle between the beams using the picomotor-controlled gimbal mirrors. Line uniformity in the images indicates minimal fringe distortion over the entire beam overlap. The picomotors can be constantly driven to write large-area gratings with continuously varying period and orientation on a substrate mounted to a precision X-Y stage. The Piezo-actuated picomotors (which produce displacement jitter and exhibit low bandwidth operation) will be subsequently replaced by voice coil-actuated fast steering mirrors.

continued

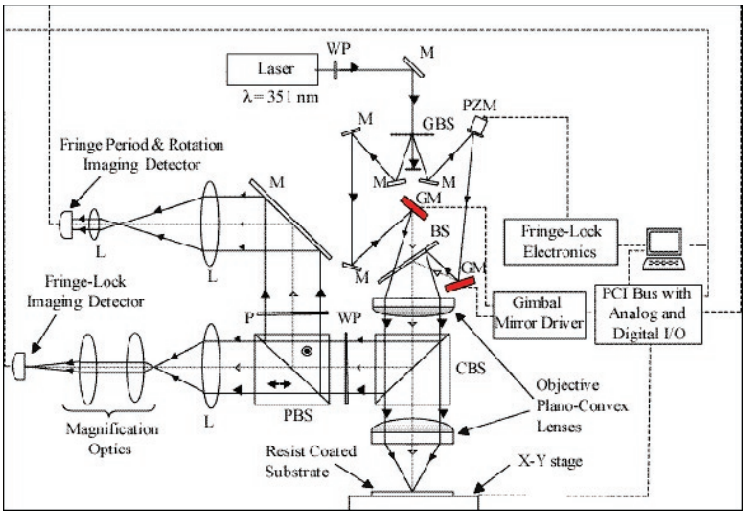

Fig. 12: Experimental diagram of variable-period scanning-beam interference-lithography system. M: mirror, L: lens, P: polarizer, GM: gimbal mirror, WP: wave plate, BS: beam splitter, PZM piezo-actuated mirror, GBS: grating BS, CBS: cubic BS, PBS: polarizing BS.

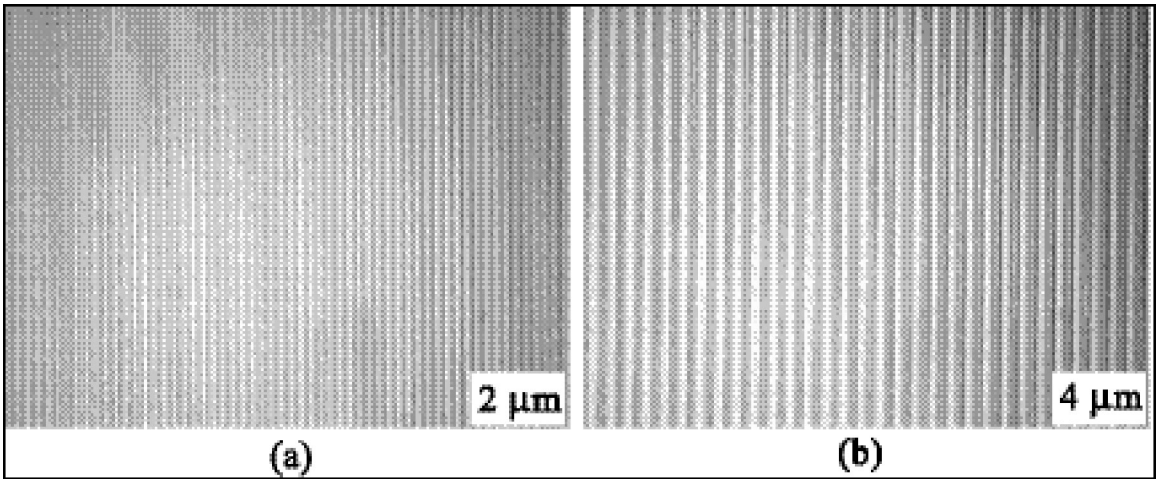

Fig. 13: Grating images written by VP-SBIL with period (a) 2.0 mm and (b) 4.0 mm.

Zone-Plate-Array Lithography (ZPAL): Lithographic Performance

Personnel
D. Gil, R. Menon, and A. Patel (H.I. Smith)

Sponsorship
DARPA and Army Research Office

In a direct-write system such as ZPAL, the major figures-of-merit are resolution and contrast. The resolution is quantified by the following equation:

(1) $$W_{min}=\lambda/NA$$

where Wmin is the minimum feature size, NA is the numerical aperture of the zone plate, lambda is the exposure wavelength, and k1 is a proportionality factor that, in effect, indicates how close to theoretical limits one operates.

In order to reduce the minimum feature size, one can increase the NA of the zone plates. The results presented in Figure 14, using NA=0.9, are the highest quality lithographic patterns ever produced with ZPAL, showing good fidelity, low edge roughness, and the ability to pattern very dense features down to the minimum spot size. It is worth noting that since all exposed pixels received the same dose, proximity effects are minimal in the exposures.

The ability to pattern curved structures and non-manhattan geometries is important for a number of applications, and our ZPAL system, by employing sub-pixel stepping, can satisfy these needs, as illustrated in Figure 15.

The minimum feature size can be further reduced by reducing k1. This corresponds to decreasing the size of the address grid, as illustrated in Figure 16.

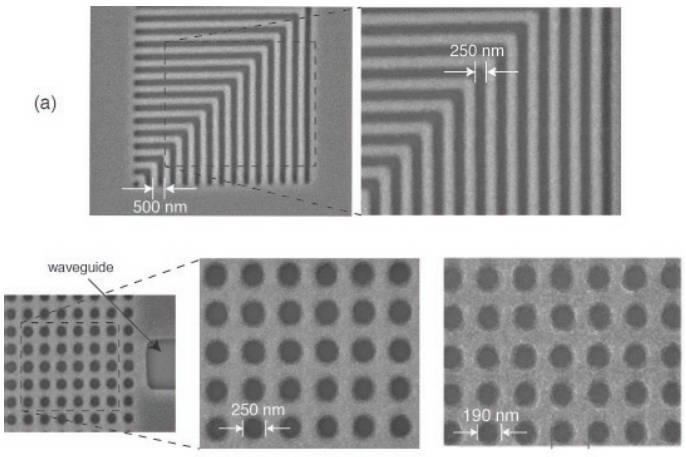

Fig. 14: Scanning electron micrographs of patterns exposed with our continuous-scan 0.9 NA UV-ZPAL system operating at λ = 400nm. (a) Dense nested Ls, (b) 2D photonic bandgap structures with 500 nm period, (c) 2D photonic bandgap structures with 360 nm period.

continued

continued

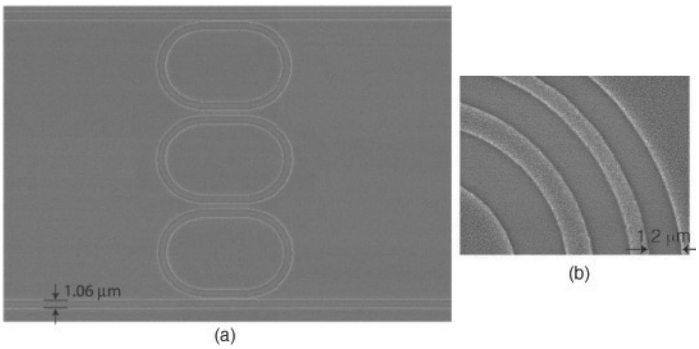

Fig. 15: Scanning electron micrographs of patterns exposed with our continuous-scan 0.9 NA UV-ZPAL system operating at λ = 400nm. Sub-pixel stepping enables patterning of curved structures with smooth edges. (a) waveguides with ring resonators, (b) one quadrant of a zone plate.

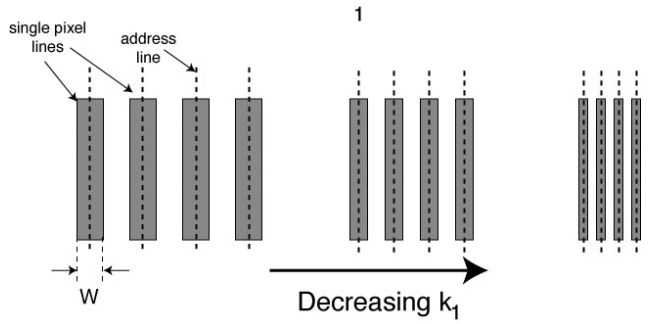

Fig. 16: k1 in ZPAL. Decreasing k1 decreases the minimum feature size. This is done by decreasing the address grid of the system, i.e., the scan lines of the focused spot are brought closer together as shown. At some point, the final image will not have sufficient contrast to be resolved by the photoresist. That point determines the limiting k1 factor.

Figure 17 shows a set of scanning electron micrographs of dense lines and spaces with varying k1's, from 0.56 to 0.38. We are currently exploring the limits of how much lower we can go, since even at k1 = 0.38 the quality of the patterning remains remarkable. Systematic characterization of lithographic exposures has also allowed us to determine that the process latitude for our current system is around 13% (even when operating at k1 = 0.38). We believe the superior lithographic performance of ZPAL is connected with the fact that there is no phase relationship between sequentially exposed spots (i.e., incoherent imaging).

Image contrast is an important lithographic-figure-of-merit. This is particularly important since phase zone plates have higher (odd) diffraction orders which contribute to the background. Here, we show that large area patterning is indeed possible with zone plates, even without order-sorting apertures, and at very high numerical apertures.

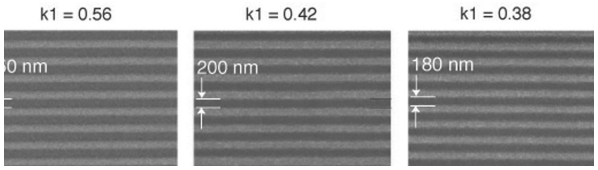

Fig. 17: Exploring the limits of k1 with ZPAL. High-numerical-aperture zone plates (0.85 and 0.9) can operate at low k1 factors (below 0.4). Sub-70 nm patterning should be possible, by operating at the demonstrated k1=0.39, with 0.9NA zone plates and λ = 157nm.

For evaluating contrast, it is sufficient to pattern full fields at the maximum resolution. Figure 16 demonstrates that full fields of dense lines and spaces can be written with high-NA zone plates. The top of the figure provides a schematic of ZPAL (without the micromechanics), illustrating the concept of parallel writing by stitching multiple fields. The bottom of the figure contains an experimental result in which we exposed fields of 125µm x 125µm (currently the scanning limit of our stage) with a 0.9 NA zone plate operating at λ=400nm and a focal length of 40 µm. A field of 125µm x 125µm corresponds to the area under a 0.85 NA zone plate, as indicated in the figure. The exposed pattern consists of 1:1 dense lines and spaces

continued

continued

with a period of 440nm. The zoomed in scanning-electron micrograph of the bottom-right of Figure 18 provides a clear view of what the pattern looks like, namely a 440nm-period dense 1:1 grating.

In summary, our results provide hard evidence that high-numerical-aperture zone plates are capable of providing sufficient contrast for state-of-the-art lithography. Although multiple diffracted orders exist, the background exposure that they produce is not deleterious. Moreover, the background can be further reduced by the utilization of order-sorting apertures.

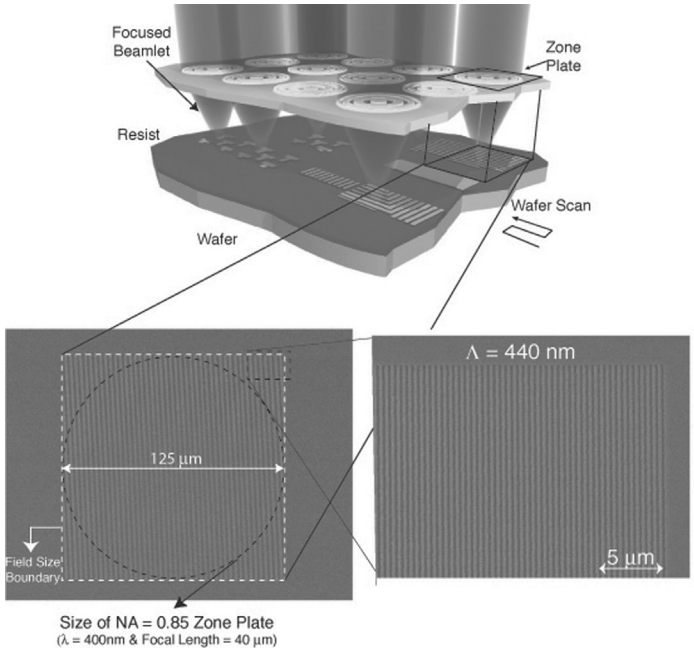

Fig. 18: Top: Schematic of the ZPAL system without the micromechanics. Large-area patterns are created by stitching adjacent fields, with a field defined as the square area located underneath any given zone plate. Bottom-left: Proof that full-field patterning is possible with ZPAL despite the existence of multiple orders. A dense 1:1, 440nm-period grating was exposed (with 400nm wavelength) covering the area of a 0.85 NA zone plate. Note that the inclined periodicity (~3μm period) observed in the left scanning-electron micrograph is the result of a moiré effect (resulting from the beating of the periodic sampling of the SEM with which the picture was acquired and the periodicity of the exposed grating. Bottom-right: Zoomed in SEM of the top-right corner of the large area grating.

X-Ray Nanolithography

Personnel
L. Chen, J.M. Daley, and E.E. Moon (H. I. Smith)

Sponsorship
DARPA and University of Wisconsin

For several years, we have been developing the tools and methods of X-ray nanolithography. We have explored the theoretical and practical limitations and have endeavored to make its various components (e.g. mask-making, resists, electroplating, sources, alignment, etc.) reliable and "user-friendly." Because of the critical importance of X-ray mask technology, we discuss this in a separate section.

X-ray NanoLithography (XNL) is a reliable and simple means of replicating patterns with feature sizes down to about 20 nm. Typically, the X-ray mask is made with Scanning-Electron-Beam Lithography (SEBL), although we very often employ a combination of interference lithography, photolithography, SEBL, and XNL to fabricate the mask. Once the mask is fabricated, it can be replicated an unlimited number of times. The simplicity and process latitude of XNL make it ideally suited for nanostructures research. In fact, at the present time, XNL is the only technique available for replicating sub-100 nm patterns of arbitrary geometry.

In the NanoStructures Lab (NSL), X-ray lithography is used in the fabrication of a large variety of structures and devices, including: photonic bandgap devices, short-channel MOSFETs, and optical channel-dropping filters.

Our sources for X-ray nanolithography are simple, low-cost electron-bombardment targets. We utilize the L line of copper at $\lambda = 1.32$ nm. The sources are separated by a 1.5 μm-thick SiN_x vacuum window from a helium-filled exposure chamber.

We have submitted a proposal to DARPA for the purchase of a laser-plasma source from JMAR, Inc. Their source operates at a wavelength of 1.1 nm which is very close to the wavelength we currently use. Figure 19 is an example of some lithography done with the JMAR source using an MIT mask. Acquisition of a JMAR laser-plasma source should enable us to reduce our exposure times from hours to minutes.

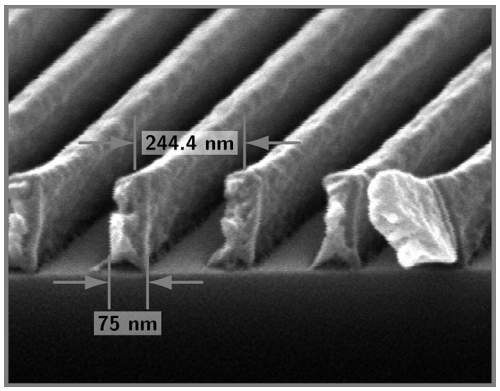

Fig. 19: Example of X-ray lithography done with the JMAR laser plasma X-ray source.

Although the wavelength used is very short (1.32 nm) compared to the minimum feature sizes of interest (e.g., 20 nm), diffraction in the gap between the mask and the substrate can be detrimental. For example, with a Cu_L source, a 50 nm feature must be exposed at a mask-to-substrate gap of less than about 4 μm in order to maintain good process latitude. A 25 nm feature would require a gap of 1 μm. For very small features, we eliminate the gap and use contact between the substrate

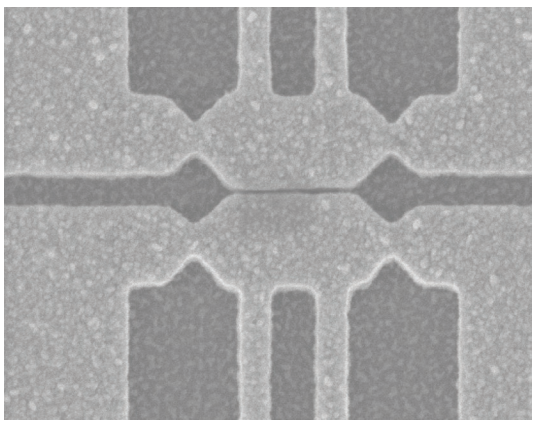

Fig. 20: Scanning electron micrographs of device pattern with feature size ~ 20 nm achieved by X-ray nanolithography.

continued

and the flexible membrane mask. This technique has enabled us to replicate features as small as 20 nm in a practical, reproducible way. Figure 20 shows scanning electron micrographs of device patterns with feature sizes less than 40 nm.

We are currently investigating if gaps below 4 μm can be reliably measured and controlled. For this, the substrate will have to be much flatter than 1 μm, something that is easily achieved with an appropriate pin chuck such as those used in optical projection lithography steppers. In fact, for the same minimum linewidth, the control of substrate flatness in X-ray lithography is less critical than in optical projection lithography by a factor 13. For a linewidth control of 10%, the control of gap in X-ray lithography is given by $\Delta G=0.2\ G$.

At linewidths of 25 nm and 50 nm, the allowable gap variation is 680 nm and 170 nm, respectively. Since the mask, if made properly, can be optically flat, the only contributor to gap variation is non flatness of the wafer or tilt of the mask relative to the wafer. We believe these can be controlled to meet the above requirements. For measuring gaps below 4 μm, we will use the "transverse chirp gapping" scheme described elsewhere in this report.

Another approach to achieving extremely fine linewidths is to use a much shorter wavelength, around 0.5 nm. At this wavelength, the high-atomic-number materials such as gold, tungsten and tantalum, and their alloys have X-ray attenuation comparable to that at a wavelength of 1 nm. The shorter wavelength enables one to use a larger gap between mask and substrate for the same resolution. The penalty one pays is that the attenuation of resist is significantly reduced, necessitating the doping of the resists with materials such as chlorine or bromine. Another issue is the energetic photoelectrons emanating from the substrate. Their deleterious effect can be eliminated by using a trilayer resist, with the bottom buffer layer absorbing the energetic photoelectrons. We are collaborating with F. Cerrina at U. Wisconsin and T. Kitayama of Mitsubishi in the development of this shorter wavelength approach.

Nanometer-level Feedback-Stabilized Interferometric Aligning and Gapping in an X-ray Lithographic System

Personnel
E. E. Moon, L. Chen, and P. N. Everett (H. I. Smith)

Sponsorship
JMAR/SAL Incorporated and University of Wisconsin

An experimental X-ray exposure system has been constructed that employs Interferometric-Spatial-Phase Imaging (ISPI) for high-precision aligning and gapping. The ISPI scheme utilizes grating and checkerboard marks on mask and substrate. When illuminated with oblique-incidence spatially-coherent light, interference patterns are formed, which are imaged by f/10 optics at a 22 degree angle from the X-ray beam at a 110 mm working distance. Since the microscopes and illumination are removed from the path of the x-ray beam, alignment and gap are detected and feedback-controlled during, as well as before, exposure.

As shown in Figure 21, each alignment mark consists of three gratings (or checkerboards), of slightly different periods, p_1 and p_2, arranged so that the two outer gratings with p_1 (on the mask) are superimposed over p_2 checkerboards (on the substrate). In the middle of the three-part mark, a p_2 grating is superimposed over a p_1 checkerboard. In this arrangement, when the mask is moved relative to the substrate, interference fringes from the middle part of the mark move in the opposite direction of the fringes from the outer parts. Alignment is determined from the relative spatial phase between the middle and outer fringe sets, measured with a sub-nanometer sensitivity frequency-domain algorithm. Phase bias due to rotation of the camera with respect to the mark is removed by examining the spatial phase difference between the two outer fringe sets.

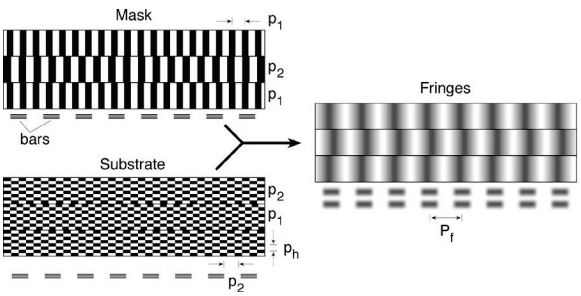

Fig. 21: Schematic of ISPI aligning marks. Fine alignment is detected using the spatial phase relation of middle to outer fringe sets. Errors from camera-mark rotation are removed by phase comparison of outer fringe sets. Spatial-phase ambiguity is eliminated by comparing the phase between bar arrays on the mask and wafer, as well as between bars and fringes.

Gap is measured from checkerboards on the mask, which have a constant period in the plane of illumination, but a varying, or chirped, period in the transverse plane. Three chirped gratings are used, with the middle chirp in the opposite direction from the outer chirps. Constant-period fringes can be obtained by design of the chirp rate. In a manner similar to that for alignment, the spatial phase of the fringes encodes gap information. In addition to phase, average intensity and fringe frequency also vary with gap. Fringe frequency variation is indicated in Figure 22, where a middle and outer fringe pair are shown at gaps of (a) 4.3 mm and (b) 19.3 mm. Fringe frequency can be used to resolve gaps to +/- 1 mm.

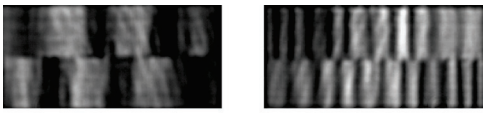

Fig. 22: Illustration of fringe variation with gap. Between (a) 4.3 mm and (b) 19.3 mm gaps the number of fringes increases by 0.51 fringe/mm.

To increase gap resolution, frequency, phase and average intensity of the transverse chip fringes are used simultaneously. The data from a gap scan between 6 and 8 μm (with 5 nm gap steps) is plotted in Figure 23(a). The same three quantities are plotted in three dimensions in Figure 23(b). The curve in Figure 23(b) traces out a highly repeatable, pseudo-helical path that indicates a unique gap within the 2-mm range. The observed gap detectivity of <20 nm is more than adequate for linewidth control of sub-50 nm features in proximity X-ray lithography.

continued

continued

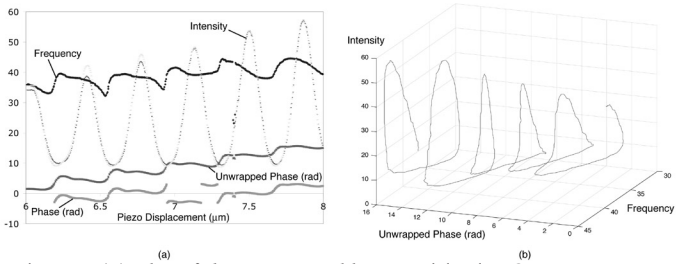

Fig. 23: (a) Plot of three measurable quantities in ISPI transverse chirp gapping fringes: frequency, phase, and average intensity as a function of gap. (b) Within the +/- 1 range of fringe frequency resolution, a unique correspondence to gap is found from a combination of all three fringe quantities. (Note that in both plots frequency is upshifted by ~4x due to zero padding.)

The same ISPI microscopes are used to detect both alignment and gap, however, alignment and gap have distinct (and conflicting) illumination requirements. Aligning is fundamentally achromatic, so any wavelength within a wide range can be used. In practice, it is advantageous to use multiple laser lines to avoid thin-film interference effects that could cause signal extinction at certain resist thicknesses. Gapping, on the other hand, is intrinsically dependent upon wavelength. Indeed, phase, frequency, and intensity in the gap marks all vary with illumination wavelength. Multiple wavelengths, if used simultaneously, would cause confusion from several sets of gap fringes. To meet both requirements, a Closed-Loop Variable Bandwidth light source (See Figure 24) is used to provide a narrow bandwidth for gapping or a broad band for aligning. The CLVB source consists of four diode lasers in the range between 635 and 690 nm, four fiber-coupled beamsplitters, and a compact spectrometer with USB computer link, which permits equalization of the power in the spectral lines during aligning, or measurement of the exact wavelength of a single laser line for gapping.

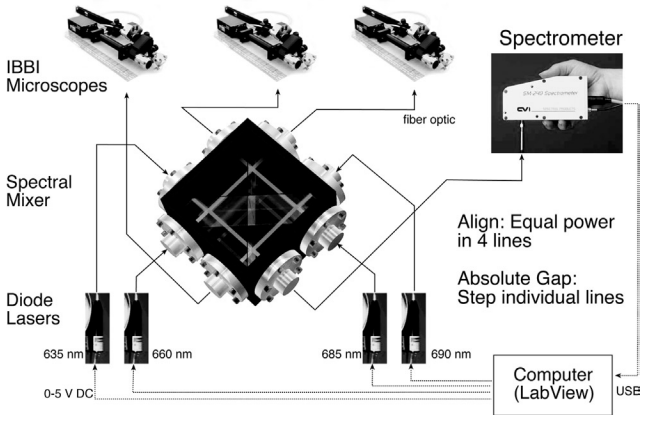

Fig. 24: A Closed-Loop Variable Bandwidth (CLVB) light source provides optimum illumination for both aligning and gapping. A single laser line is used for gapping, but a broad spectrum using multiple lasers is ideal for aligning. The spectrometer monitors wavelength when gapping, and relative intensities when aligning.

The unique collection of capabilities inherent to ISPI aligning and gapping is being employed in the fabrication of a variety of electronic and optical devices.

Adaptive-Membrane-Mask Technology

Personnel

J.M. Daley and T.B. O'Reilly (G. Barbastathis and H. I. Smith in collaboration with M. Feldman, LSU)

Sponsorship

DARPA/Naval Air Systems Command and Louisiana State University

The conventional approach to maintaining pattern fidelity and overlay in lithography is to minimize distortion in pattern generation and transfer, and to make masks as rigid as possible. Since July 2000, we have been pursuing a radically new approach that seeks to exploit the flexibility of membrane masks. This approach, which we call the Adaptive Membrane Mask (AMM), seeks to actively measure and control mask distortion, making it possible to eliminate or compensate for many types of distortion common in lithography. This approach is similar in spirit to adaptive optics where optical surfaces are actively deformed to compensate for system or media distortions.

Our approach to distortion measurement is based on holographic interferometry. A reference grid is fabricated on the back of a membrane mask using Interference Lithography (IL). Mask distortion is measured using the Holographic-Phase-Shifting Interferometer (HPSI), shown in Figure 25, essentially an IL system modified to measure in-plane distortion of the reference grid on the membrane. We believe that HPSI will be able to measure in-plane distortion of the mask with resolution of the order of 1 nm.

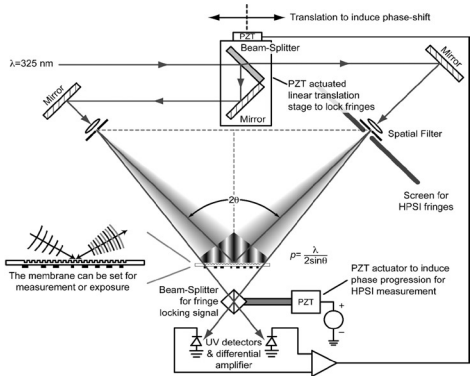

Fig: 25: Schematic of the Holographic-Phase-Shifting Interferometer(HPSI). This setup can be used as an interference lithography system to write reference grids as well as a holographic interferometer to measure grid distortion.

Once the distortion is measured, an algorithm developed at MIT is used to calculate the temperature distribution that will generate thermal stresses to eliminate the measured distortion. The membrane mask is heated using a computer-controlled illumination source, based on either a spatial light modulator, such as the Texas Instruments digital micromirror array, or a scanned laser system. The distortion is measured again, and the process is repeated iteratively until the distortion is eliminated. The final temperature distribution is measured using an infrared camera. The

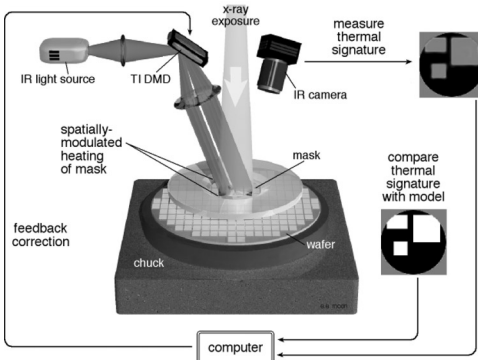

Fig. 26: Proposed implementation of Adaptive-Membrane-Mask Distortion Correction

proposed implementation is outlined in Figure 26. Because membrane distortion is directly related to temperature, it can be eliminated by maintaining this final temperature distribution.

The AMM approach is ideally matched to X-Ray Lithography (XRL). The primary sources of distortion in XRL are distortion of the mask due to stresses in the absorber layer and by radiation damage. XRL membrane masks used in industry are typically 2 microns thick silicon carbide, which is not subject to radiation damage at exposure levels seen in industry. The ability to measure and correct distortion may allow

continued

the use of a wider range of materials for both membrane and absorber, and relax some process constraints currently needed to minimize absorber stress. For instance, masks can be made from silicon nitride, which is less expensive and easier to make than silicon carbide, but is subject to radiation-damage-related distortion. The use of thinner membranes has the additional advantage of reducing exposure times and increasing optical transmission for mask alignment.

An AMM can be used to provide magnification correction. AMM can also be used to correct for wafer distortion, which can arise from a number of causes: high temperature processing, stress in grown overlayers, stress due to ion implantation, etc. As long as these distortions are measurable and repeatable, an adaptive mask can compensate for them, allowing more flexibility in wafer processing. For example, high temperature processes that induce wafer distortion can be used since the AMM can compensate for them. The advantages described above also apply to the use of AMM with types of lithography other than XRL that use membrane or stencil masks, including electron, ion- and neutral-atom lithography. In addition, we believe that adaptive masks may be applicable to Optical-Projection Lithography (OPL), by far the dominant technique for fabricating semiconductor chips. Although rigid masks are currently used in OPL, reducing the importance of distortion in the mask, OPL is subject to all of the other types of distortion described above. In addition, the projection lens system introduces distortion in the image produced on the substrate. Application of AMM to OPL should allow control of this distortion and may allow the use of simpler projection lens systems.

Preliminary work has shown good agreement between experiment and model. Figure 27 compares experimental and analytical results for a simple case where the left half of the membrane is heated. Here, displacements are plotted along a horizontal line in the middle of the membrane.

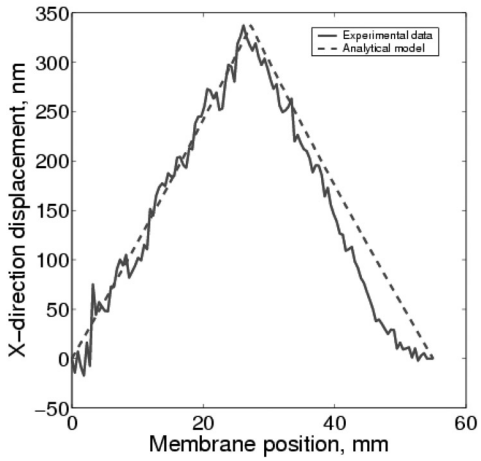

Fig. 27: Comparison of experimental and analytical results

Interference Lithography

Personnel

J.M. Carter, R.C. Fleming, T.A. Savas, M.E. Walsh, and T.B. O'Reilly (M.L. Schattenburg and H.I. Smith)

Sponsorship

DARPA and U.S. Army Research Office

Interference Lithography (IL) is the preferred method for fabricating periodic and quasi-periodic patterns that must be spatially coherent over large areas. IL is a conceptually simple process where two coherent beams interfere to produce a standing wave, which can be recorded in a photoresist. The spatial-period of the grating can be as low as half the wavelength of the interfering light, allowing for structures of the order of 100nm from UV wavelengths; features as small as 30-40 nm are also possible using a DUV ArF laser.

The NanoStructures Lab has been developing IL technology for close to 20 years, and we currently operate 4 different IL systems for a wide variety of applications. One system, shown schematically in Figure 28, is run in cooperation with the Space Nanotechnology Lab. This system is specially designed for high stability and repeatability and is capable of producing metrological quality gratings and grids up to 10 cm in diameter at spatial periods down to 200nm. Used primarily for satellite applications, gratings produced with this tool have flown on numerous missions, most notably, the Chandra X-ray astronomy satellite launched in August of 1999, which included hundreds of matched, high-precision gratings.

We operate another system similar to the one shown in Figure 28 based around the 325 nm line of a HeCd laser. This system functions both as an exposure tool with capabilities comparable to those described above as well as an analysis tool. Using a technique known as Holographic Phase-Shifting Interferometry (HPSI), the linearity and spatial phase of gratings produced in this system can be quantitatively measured and mapped with an accuracy on the order of parts per million. Known hyperbolic distortions in the spatial-phase of gratings printed using IL are responsible for changes in periodicity of a few angstroms (for a 200nm period grating) over a 10 cm wafer. Although seemingly small, distortions of this scale can be highly

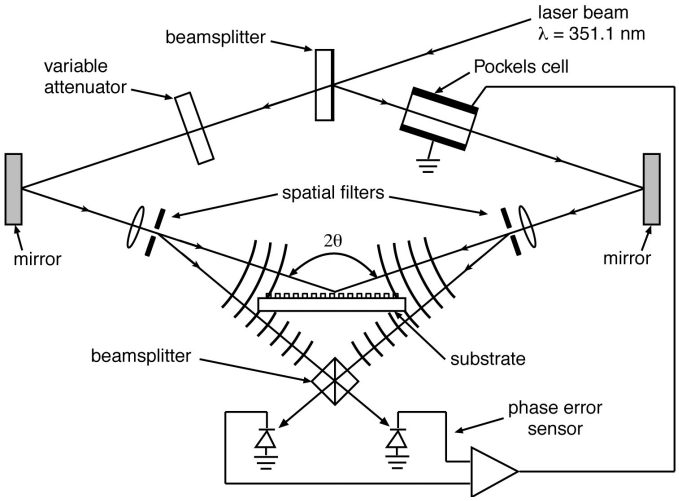

Fig. 28: Schematic of one of the MIT interferometric lithography systems. This system occupies a 2x3m optical bench in a class 100 clean environment. The beamsplitter directs portions of the two interfering spherical beams to photodiodes. A feedback locking is achieved by differentially amplifying the photodiode signals and applying a correction to the Pockels cell which phase shifts one of the beams in order to stabilize the standing wave pattern at the substrate.

significant, especially in metrological applications such as the fiducial grids for spatial-phase locked electron beam lithography. Using the HPSI, we have been able to investigate innovative techniques for reducing these distortion levels. One method, based on the controlled bending of the substrate during exposure, has demonstrated a reduction of the distortion pattern from 2 dimensions to 1 dimension as well as reducing the magnitude of the distortions by about a factor of 5.

Also utilizing a 325 nm HeCd laser is the Lloyds-mirror interferometer, shown schematically in Figure 29. The primary advantage of the Lloyds-mirror is that the spatial-period of the exposed gratings can be easily and continuously varied from many microns down to ~170 nm simply by rotating the stage without realigning the

continued

continued

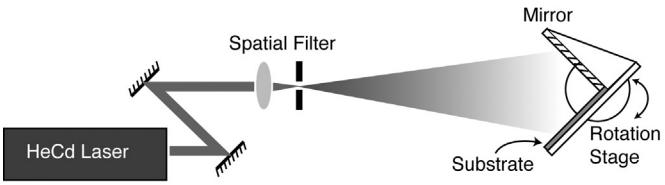

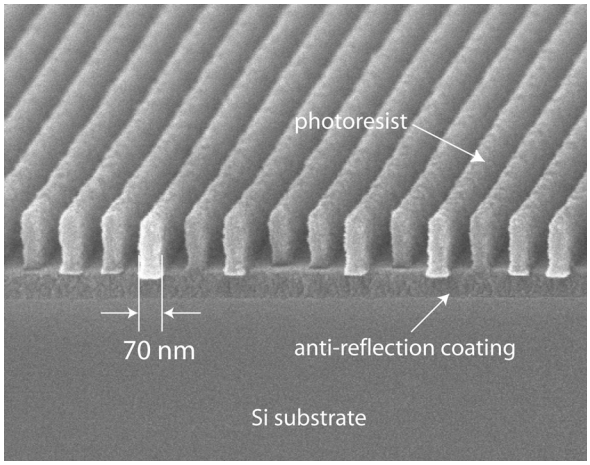

Fig. 29: Schematic of a Lloyds-mirror interferometer. The substrate and mirror are fixed at a 90˚ angle to one another, and centered in a single incident beam. Rotating the substrate/mirror assembly about its center point varies the spatial-period of the exposed grating. The micrograph shows a grating with 70 nm lines on a 170 nm pitch exposed using the Lloyds-mirror.

optical path. This has opened the door to new possibilities such as varied aspect-ratio grids (different periodicities in the two axes of the grid) for patterned magnetic media and MRAM (Magnetic Random Access Memory) devices. Among the many other applications of IL supported by the Lloyds-mirror are alignment templates for organic crystals and block co-polymers, semiconductor quantum dots, and other self-assembling structures.

Distributed FeedBack (DFB) structures for quantum dot lasers and photonic bandgap devices have also been made using the Lloyds-mirror.

For spatial periods of the order of 100 nm, we use a 193 nm ArF laser. To compensate for the limited temporal coherence of the source, we utilize an achromatic scheme shown in Figure 30. In this configuration the spatial period of the printed grating is dependent only on the period of the parent gratings used in the interferometer, regardless of the optical path or the wavelength and coherence of the source. Thus, gratings and grids produced with this tool are extremely repeatable. Figure 31 shows a 100 nm-period grid of 13 nm-diameter posts etched into Si, produced using Achromatic Interferometric Lithography (AIL) and a sequence of etching steps. Other applications AIL include patterned magnetic media, gratings for atom-beam interferometry UV polarizers, and templated self-assembly.

A new generation of achromatic interference lithography tools is currently being developed to produce 50 nm period gratings and grids, or 25 nm lines and spaces. Because of the limited availability of sub-100nm wavelength sources, all of the possible implementations for making 50 nm period gratings are based around the achromatic scheme described for 100 nm period gratings. Among the possibilities are free-standing gratings etched in a thin membrane for use with soft X-rays, or use of reflection gratings in an analogous AIL scheme with a 58.4 nm helium discharge.

The fourth type of interference lithography is Scanning-Beam Interference Lithography (SBIL). Such a system, which is also called the Nanoruler, has been constructed in the Space Nanotechnology Laboratory, and is described in another section.

continued

continued

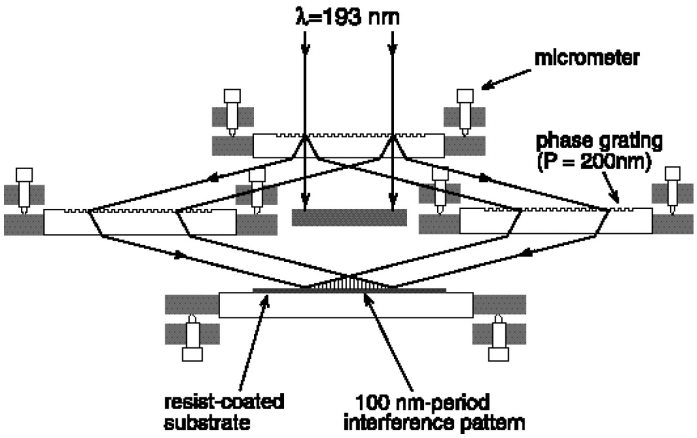

Fig. 30: Achromatic interferometric lithography (AIL) configuration employed to produce 100 nm-period gratings and grids.

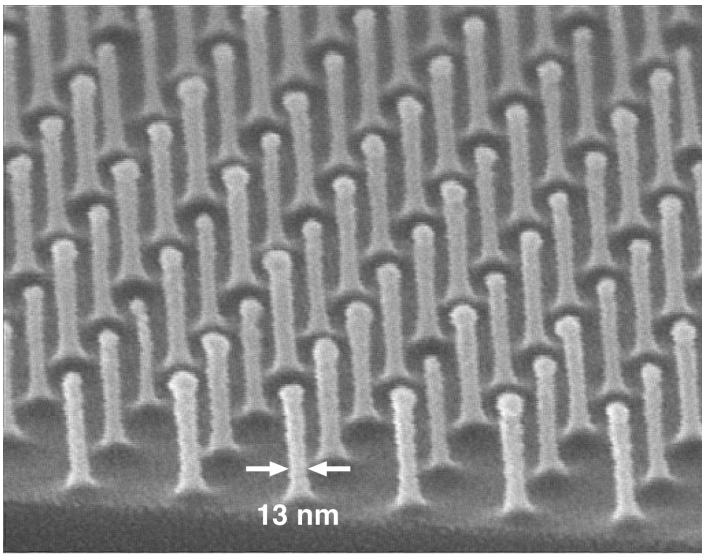

100nm-period posts in Si

Fig. 31: Scanning electron micrograph of a 100 nm-period grid, exposed in PMMA on top of an antireflection coating, and transferred into Si by reactive ion etching.

The MIT Nanoruler:
A Tool for Patterning Nano-Accurate Gratings

Personnel
C. Chen, C.-H. Chang, C. Joo, P. Konkola, J. Montoya, and Dr. R. Heilmann
(M. L. Schattenburg and H.I. Smith)

Sponsorship
DARPA, Army Research Office, and NASA

Historically, the ability to observe and measure the results of processes has been critical to advancing fabrication technology. Thus, improvements in optical microscopy (e.g., Nomarski differential interference contrast) were a key enabler of the microelectronics revolution. In turn, the scanning-electron and atomic-force microscopes are essential tools as we move into the nanotechnology era. While the ability to print or resolve a particular feature size is a necessary condition for the successful lithographic manufacturing of nanosystems, it is, by no means, the only requirement. Equally important is the ability to measure and control the size and placement of lithographic features with very high accuracy

All modern lithographic production and inspection tools, and all precision tools for that matter, are based on the notion of a metrology frame. Such a frame is composed of three components: (1) a rigid mechanical structure, (2) means to measure the motion of a workpiece with respect to the metrology frame, and (3) means to project, image or detect patterns on the workpiece, such as by use of an optical or electron lens. The preferred means for measuring workpiece motion has been the laser interferometer. The accuracy of a lithographic tool is critically dependant on the accuracy of its metrology frame, which, in turn, is dependant on the accuracy of the interferometer. Due to a number of complex factors, however, interferometer accuracy is not keeping pace with the shrinking tolerances as called for by the semiconductor industry roadmap (See Figure 32) and the future nanotechnology revolution.

To address this problem, we are developing a lithographic tool called the Nanoruler that is designed to pattern gratings of such high accuracy that they may serve as the means for detecting workpiece motion in precision tools, using a method known as optical encoding, with an accuracy that is some 10-100X better than laser interferometers. The Nanoruler utilizes a patterning method called Scanning-Beam-Interference Lithography (SBIL), developed in the Space Nanotechnology Laboratory (SNL), that is capable of rapidly patterning large gratings (>300 mm diameter) in only a few minutes with unprecedented accuracy (see Figure 33). Such super-accurate gratings can serve as optical encoder plates, as mentioned. Another important application for the Nanoruler is the patterning of nano-accurate gratings necessary for locking an electron beam using a novel technique called Spatial-Phase Locked Electron Beam Lithography (SPLEBL) that is under development in the NanoStructures Laboratory (NSL) and described elsewhere.

High fidelity gratings are also critical for advanced instrumentation and optics such as laboratory and astronomical spectrographs, high-bandwidth optical communications and fusion energy research. Conventional means of fabricating gratings, such as diamond ruling, holography, or beam writing, can take many hours or weeks to complete, and typically produce gratings of poor spatial-phase fidelity.

The concept of SBIL is to combine the sub-1 nm displacement-measuring capability of laser interferometry to control a high-performance air-bearing stage, with the interference of narrow coherent beams, to produce coherent, large-area, linear gratings and grids. Our ultimate goal is to produce gratings with sub-nm distortion over areas many tens of centimeters in diameter. SBIL requires sophisticated environmental controls to mitigate the effects of disturbances such as acoustics, vibration, and air turbulence, and variations of temperature, pressure, and humidity. The system also features real-time measurement and control of optical phase using heterodyne fringe detection, acousto-optic modulator phase locking (See Figure 34), and a high-speed Digital Signal Processor (DSP) controller (See Figure 35).

continued

continued

An important feature of SBIL is the ability to both write and read gratings with nanometer control of grating phase. Figure 36 is a map of phase error for a grating that was first written in the Nanoruler, developed, and then placed back into the tool and read. The data demonstrates ~2 nm 3s repeatability of the writing/reading process, which includes errors due to substrate chucking/unchucking.

YEAR	2001	2002	2003	2004	2005	2006	2007	2010	2013	2016
CD (nm)	130	115	100	90	80	70	65	45	32	22
OVERLAY (nm, mean+3 sigma)	45	40	35	32	28	25	23	18	13	9
MASK IMAGE PLACEMENT (nm)	27	24	21	19	17	15	14	11	8	6
	Solutions Exist			Solutions Being Pursued			No Known Solutions			
METROLOGY FRAME ERROR (nm)	11	10	8.8	8.0	7.0	6.3	5.8	4.5	3.3	2.3
LENGTH SCALE ERROR (nm)	2.8	2.5	2.2	2.0	1.8	1.6	1.4	1.1	0.8	0.6
	MIT Effort									

Fig. 32: Semiconductor Industry Association (SIA) roadmap tracking Critical Dimension (CD) or minimum feature size, overlay error, mask image placement error, and metrology tool error. The MIT effort seeks to produce grating metrology standards with sub-nm errors, which would be used as planar metrology length scales or optical encoders in lithographic and other equipment, eliminating the laser interferometer.

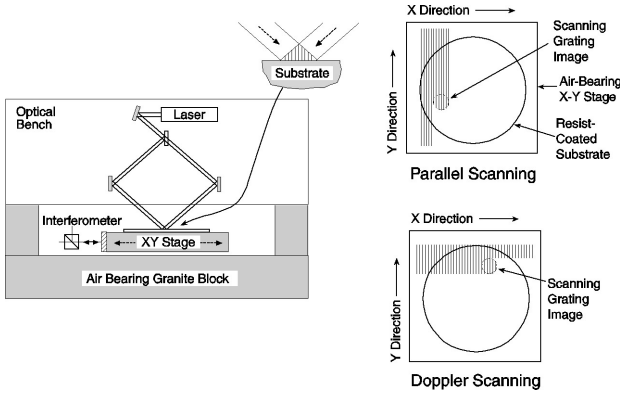

Fig. 33: Schematic of the Scanning-Beam-Interference-Lithography (SBIL) system under development in the SNL. A pair of narrow, low-distortion beams overlap and interfere at the substrate, producing a small grating "image." The substrate is moved under the beams, writing a large area grating. Tightly overlapped scans ensure a uniform dose.

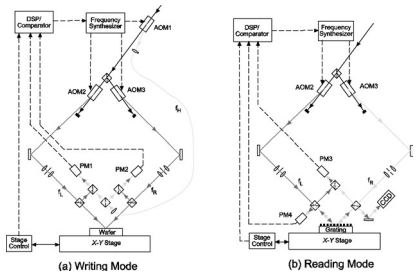

Fig. 34: Schematic of SBIL Acousto-Optic (AO) modulator phase locking system. Both writing and reading modes are depicted. The phase of the grating image is measured by a small interferometer close to the writing surface. The AO modulators Doppler shift the beams into the megaHertz range, providing high-accuracy heterodyne measurement of phase. This information is processed by a digital signal processor and used to control RF frequency synthesizers which drive the AO modulators, thus locking the image phase to the moving substrate.

continued

continued

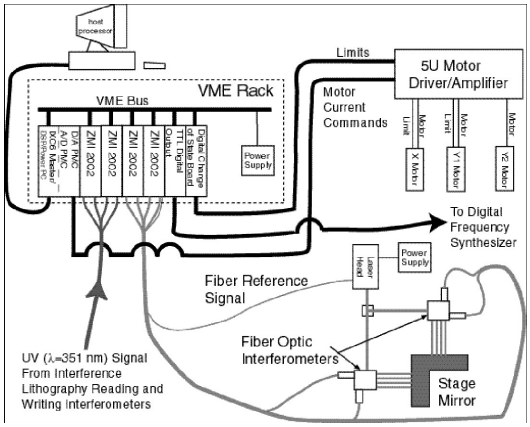

Fig. 35: Schematic of SBIL system control architecture. The system utilizes a frequency stabilized HeNe laser (l=632.8 nm) and heterodyne interferometry to measure substrate position, and argon ion laser (l=351.1) heterodyne interferometery to measure image fringe phase. Phase error signals are processed by an IXTHOS 4x167 MHz DSP board which then drives the stage DC motors and the RF digital frequency synthesizer controlling the fringe-locking AO modulators.

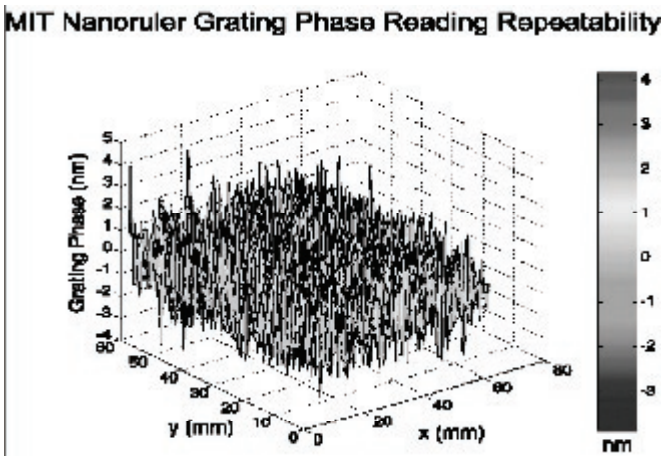

Fig. 36: Wafer phase mapping repeatability (nm), for a 400 nm-period grating that was written and then read by the Nanoruler.

Templated Self-Assembly

Personnel

K. Nielsch, M. Walsh, and A. L. Giermann (C. A. Ross, H. I. Smith, C. V. Thompson in collaboration with F. Ross, IBM, and F. Frankel, MIT)

Sponsorship

NSF

Self-organizing systems can be used to create fine-scale periodic patterns with good short-range order. However, the long-range order of such patterns is typically poor, limiting their usefulness in nanoscale structures or devices. In this new project, methods are being developed to induce long-range order in self-assembled systems patterning the substrate with a lithographically defined periodic structure. This approach is called 'templated self-assembly'. Patterning is carried out by topographically or chemically modulating a substrate, using interference lithography which can pattern large areas of a substrate with periodic features of ~100 nm dimension. The periodically-modulated substrate then provides long-range order to the self-organized system. The overall goal of the project is to develop methods by which nanoscale patterns can be created using a combination of 'conventional' lithography and self-assembly. Of particular interest is how the quality of the assembly is affected by the relative length-scales of the template and the natural period of the self-assembled system.

This approach is being applied to several different physical systems in order to understand how different types of substrate modulation can be used to create nanostructures with long-range order. Examples include the phase-separation of block copolymers (see under 'Block Copolymer Lithography'), the formation of pores in alumina during anodization, the growth of strained SiGe quantum dots on Si substrates by chemical vapor deposition, and the agglomeration ('dewetting') of metal films on oxide surfaces. An example is shown in Figure 37 which illustrates how the pores in anodized alumina, which typically form with a hexagonally-close-packed arrangement, can be formed instead in a square array. This is achieved by depositing an aluminum film over a substrate that has been patterned with a square array of pyramidal indentations, created by interference lithography and anisotropic etching.

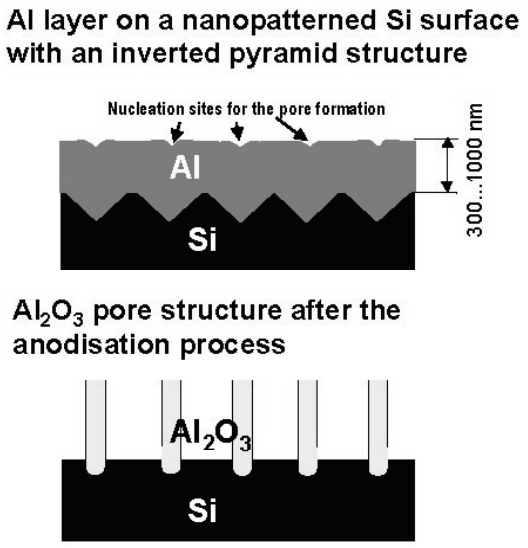

Fig. 37: To make a film of anodized alumina containing a regular arrangement of pores, we start by patterning a silicon substrate with a square array of inverted pyramids, using interference lithography. The substrate is then coated with Al, which conforms to the surface topography. The aluminum film is then anodized (at 80V in this case), and the indentations in the aluminum act as nucleation sites for pores. A film of porous alumina grows containing a square array of pores.

Block Copolymer Lithography

Personnel

J. Cheng and G. J. Vancso (C. A. Ross, H. I. Smith, and E. L. Thomas)

Sponsorship

NSF through the MIT Center for Materials Science and Engineering

Fabrication of large-area periodic nanoscale structures using self-organizing systems is of great interest because of the simplicity and low cost of the process. Block copolymers consist of polymer chains made from two chemically distinct polymer materials. These can self-assemble to form small-scale domains whose size and geometry depend on the molecular weights of the two types of polymer and their interaction. The domains have a very uniform distribution of sizes and shapes. We have been using block copolymers as templates for the formation of structures such as magnetic particles by selectively removing one type of domain and using the resulting template to pattern a nanostructured magnetic film. An example is shown in Figure 38, where Co dots have been made using ion milling to pattern a Co film. The structure has a center-to-center spacing of 50 nm.

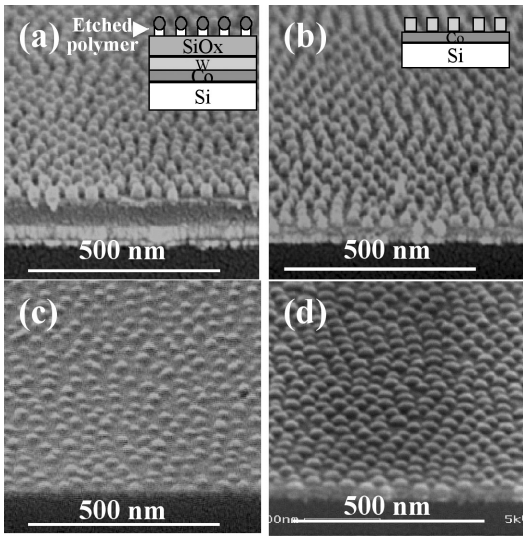

Fig. 38: Cross-section SEM micrographs of (a) Block copolymer lithographic template on the multilayer film. (b) W hard mask (dots) on continuous Co film. (c) Co dots after Ar ion milling. (d) Co dots after Ne ion milling.

However, the self-assembled block copolymer lacks long-range order (See Figure 39(a)). Graphoepitaxy is used here to induce orientation and positional ordering of the block copolymer through an artificial surface patterning. Block copolymers have been spin-cast on silica grating substrates made by interference lithography. For block copolymer PS/PFS 50/12, well-ordered structures form in the grooves of the gratings with all the close-packed rows aligned within the grooves (See Figure 39(b)), provided the groove width is comparable to the 'grain size' of the block copolymers. We have found that the number of rows within the groove, the spacing of the rows, and the deliberate introduction of defects such as vacancies and dislocations can be controlled by adjusting the groove dimensions. These ordered nanostructures may be useful as templates for various applications.

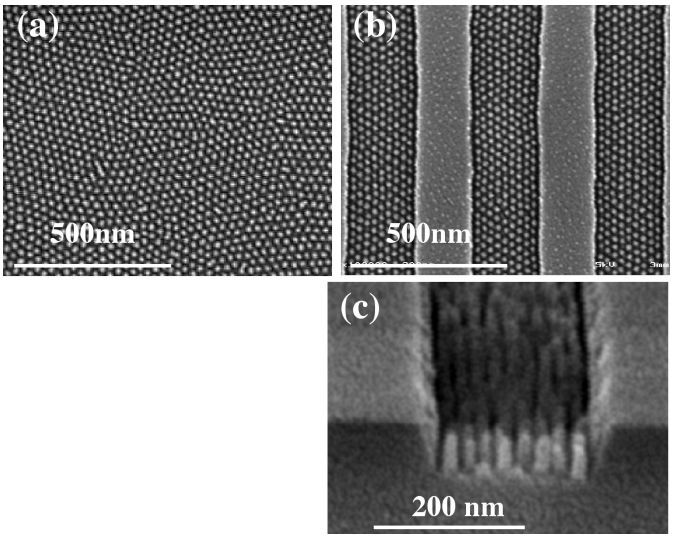

Fig. 39: (a) PS/PFS block copolymer 50/12 on the flat silica substrate. (b) PS/PFS 50/12 forms an ordered structure in 260nm wide silica grooves fabricated by interference lithography. (c) Ordered array of silica pillars, formed by etching using the ordered block copolymer as a template.

Precision Fabrication Techniques for Microphotonic Devices

Personnel

T. Barwicz, J.T. Hastings, J. Huang, M.J. Khan, and M.H. Lim (H. Haus and H.I. Smith)

Sponsorship

DARPA and U.S. Army Research Office and Pirelli Lab S.p.A.

Microphotonic devices seek to miniaturize and integrate the components needed for optical networking. These devices have exacting fabrication tolerances for feature size, pattern-placement, and surface roughness. Careful control of feature size is critical for resonant structures and phase-matching between coupled waveguides, while pattern-placement is essential for devices that rely on long-range interference effects. Surface roughness often dominates optical loss in a device. As a result, only careful control of the fabrication process can maximize device performance. This project focuses on Bragg-grating-based devices and high- index-contrast devices; both of which require precision fabrication.

Grating-Based Devices

Bragg-gratings have widespread application in the field of optical telecommunications. A Bragg-grating is formed by creating a periodic corrugation or refractive index modulation in an optical waveguide. Such a structure behaves as a wavelength-selective filter, reflecting a narrow band of wavelengths while transmitting all other wavelengths. Although Bragg-gratings are commonly imprinted in photosensitive optical fiber, physically-patterned gratings in planar waveguides, shown in Figure 40, offer a number of advantages. For example, one can build Bragg-gratings in non-photosensitive materials such as indium phosphide or silicon. In addition, integrated gratings can contain precise phase-shifts and variations in grating strength to achieve a desired filter response. Finally, the planar-fabrication process can integrate multiple gratings with splitters, couplers, and other optoelectronic components on a single, readily manufacturable chip.

We use a combination of several different types of lithography to generate Bragg-grating devices. In interference lithography, two coherent laser beams are crossed, generating a standing-wave interference pattern. This standing-wave pattern is used to expose photoresist, yielding a coherent submicron-period grating. This grating can be used directly as the device grating or it can serve as a precision reference for later electron-beam lithography steps.

For devices that require long Bragg-gratings with engineered phase shifts or variations in grating strength, we use a technique called Spatially-Phase-Locked E-Beam Lithography (SPLEBL), which combines the long-range spatial coherence of interference lithography with the flexibility of scanning e-beam lithography. Inherent pattern-placement errors in gratings written by standard e-beam lithography limit device performance. SPLEBL references the interference-generated grating during the e-beam exposure to minimize these placement errors.

In many cases, the techniques mentioned above are not applied directly to a device, but instead to an X-ray lithography mask. Once the mask is generated, with the appropriate gratings and alignment marks, the patterns can be repeatedly transferred to substrates using X-ray lithography.

One of the critical challenges facing integrated Bragg-gratings is that they often require submicron grating structures patterned over relatively tall optical waveguides. In order to address this topography problem, we have developed a dual-hardmask process, depicted in Figure 44. This process allows both lithography steps to be performed over essentially planar surfaces. Figure 43 shows devices fabricated by the dual-hardmask process in the indium-phosphide and silicon-on-insulator materials systems.

In many cases it is desirable to place Bragg gratings in the sidewalls of optical waveguides as shown in Figure 43 (b). This technique allows the grating and waveguide to be patterned in the same lithographic step. As a result, the grating depth can be easily varied along the waveguide to introduce apodization. Apodization, the process of gradually increasing and

continued

continued

then decreasing the grating strength, reduces side-lobe levels in the reflection and transmission spectra of the device, thus reducing cross-talk between neighboring channels in wavelength-division multiplexing. Figure 43 (a) shows an apodized-sidewall grating in a SOI ridge waveguide along with measured transmission spectra. The waveguide-grating structures were patterned using Spatial-Phase-Locked E-Beam Lithography (SPLEBL) and chlorine reactive ion etching. The silicon-on-insulator substrates were provided by Canon.

High Index-Contrast Devices

High-refractive-index-contrast-material systems enable very small bending radii in microphotonic devices. In low-index-contrast waveguides (such as optical fibers), the bending radii must be on the order of centimeters. On the other hand, integrated-optical waveguides exploiting the high index contrast between Silicon Nitride and Silicon Oxide may have bending radii on the order of 10um. This is 1000 times smaller. Consequently, device size shrinks considerably, and large-scale integrated optical circuits become possible. Unfortunately, fabrication of high-index-contrast microphotonic devices is much more demanding than fabrication of low-index-contrast ones. The main challenges reside in precisely and accurately controlling dimensions of submicron features as well as in achieving the required smoothness of waveguide sidewalls. High-index-contrast microphotonic devices are much more sensitive to feature size variations. Moreover, scattering losses due to sidewall roughness become increasingly important when index contrast goes up and may even render devices unusable. In the NanoStructures Laboratory, dimensional control is addressed by using direct-write scanning-electron-beam lithography. The higher resolution allows for much better control of submicron features than photolithography. Sidewall roughness is addressed by optimizing reactive-ion etching for minimal mask erosion (See Figure 44). Additionally, quantitative sidewall roughness measurement techniques are developed for efficient optimization and monitoring of fabrication processes.

An add-drop filter based on optical racetrack resonators is shown on Figure 46. Light is evanescently coupled from a bus waveguide to an adjacent racetrack. If the optical path in a racetrack is equal to an integer number of wavelengths, one will have resonance. In this case, power will be entirely transferred from one bus waveguide to the racetracks and then to the other bus waveguide. The resonance has a Lorentzian profile for a single racetrack and becomes sharper if multiple racetracks are used. The whole device occupies about 20 by 50 μm while low-index-contrast add-drop filters require millimeters or even centimeters.

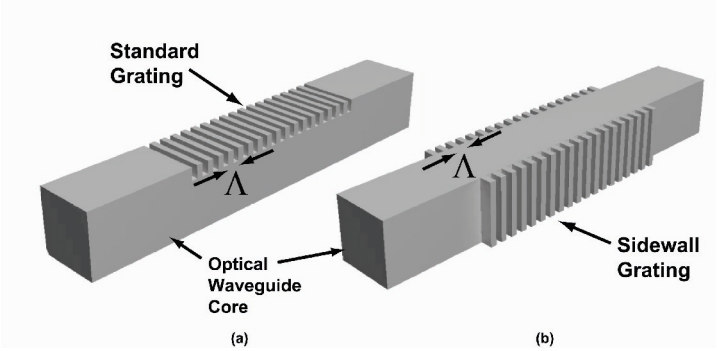

Fig. 40: Two possible configurations for physically patterned Bragg gratings in optical waveguides. (a) Bragg grating patterned in the top of the high-index core. (b) Bragg grating patterned in the sides

continued

continued

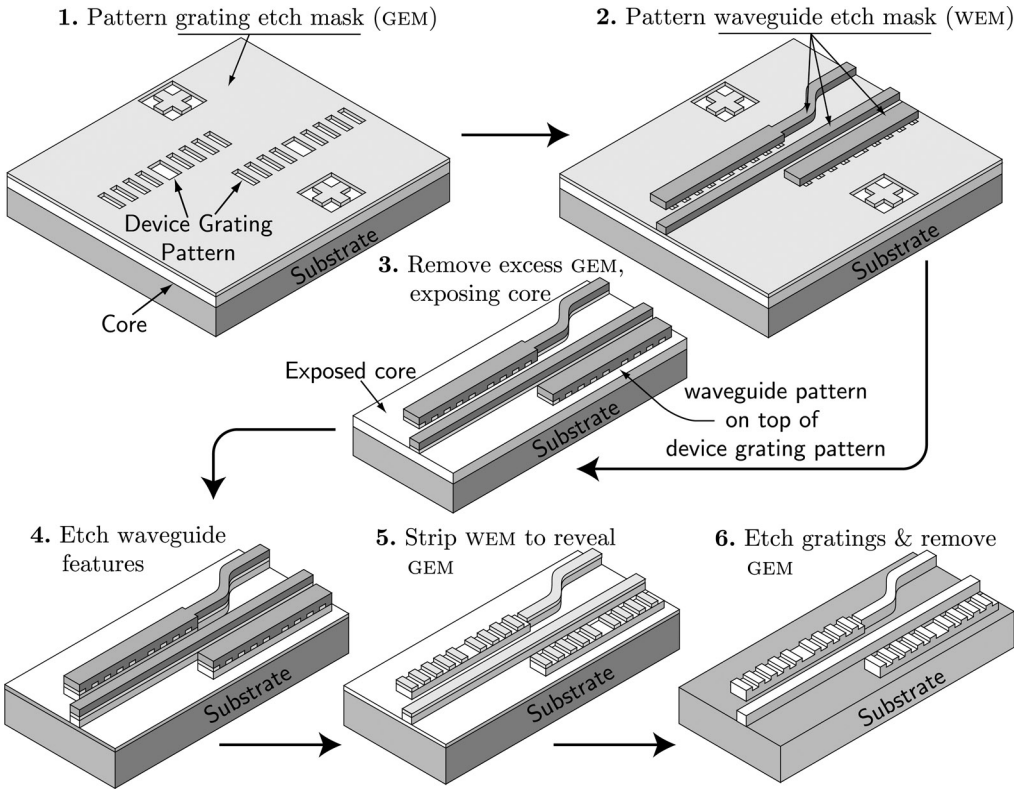

of the high-index core.

Fig. 41: Dual-hardmask process used to pattern fine-period Bragg gratings atop relatively tall waveguide structures. The process is designed such that all lithography steps are performed over essentially planar topography.

continued

continued

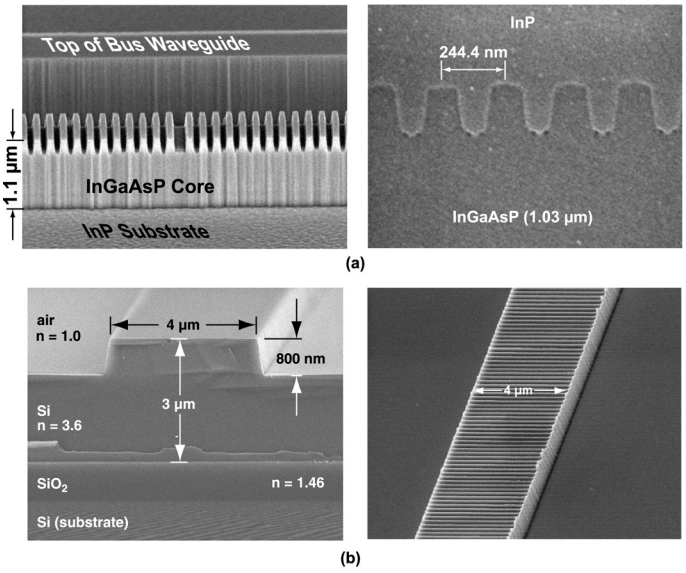

Fig. 42: Examples of the dual-hardmask process applied to two different materials systems. (a) Scanning-electron micrograph depicting a quarter-wave-shifted, 244.4 nm period Bragg grating etched into the top surface of an InGaAsP waveguide, and the subsequent InP overgrowth. (b) Silicon-on-insulator (SOI) ridge waveguide cross-section and SOI waveguide with Bragg grating in the top.

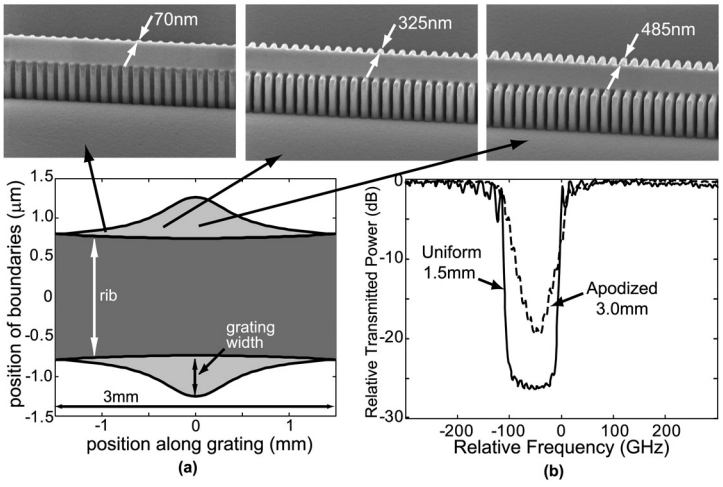

Fig. 43: (a) Apodized Bragg gratings fabricated in the side-walls of a SOI ridge waveguide. (b) Transmission specta for the TE- mode of uniform and apodized waveguide-grating devices. The reduction of side-lobe levels for the apodized devices is readily apparent.

continued

continued

Fig. 44: Cross-section of a high-index-contrast waveguide with smooth sidewalls. Light is guided by the 330nm thick Silicon-rich Silicon Nitride (SiN) layer with an index of refraction of 2.20. The Silicon Oxide layer is about 3 microns thick and acts as optical isolation from the Silicon wafer.

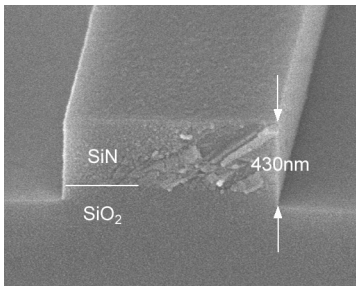

Fig. 45: Add-drop filter based on optical racetrack resonators. This structure was fabricated using scanning-electron-beam lithography. For high-volume manufacturing, a high-resolution replication technique such as X-ray lithography could be used.

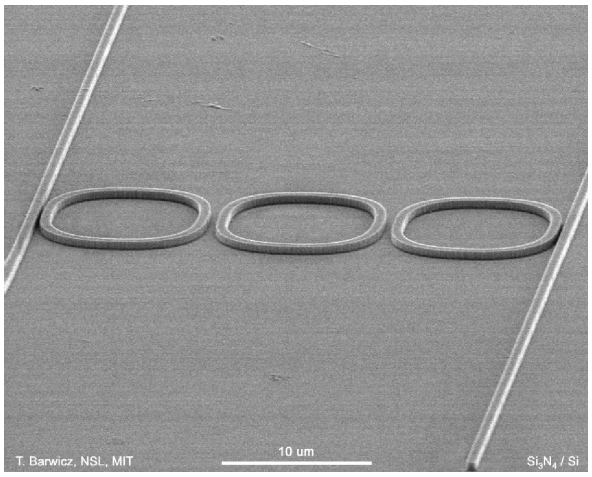

Nanopattern-Assisted Growth of Organic Materials for Device Applications

Personnel

D. Mascaro and J. Zartman (V. Bulovic)

Sponsorship

MARCO Focused Research Center on Materials, Structures, and Devices (MARCO/DARPA)

While optoelectronic devices based on organic small molecules have recently become commercially available, electronic devices such as field-effect transistors are less well developed. Typical Organic Field-Effect Transistors (OFET) utilize polycrystalline thin films of evaporated organic materials such as pentacene as the semiconducting layer. The charge carrier mobility, and hence performance, in pentacene OFETs is primarily determined by the molecular ordering within the thin film, where the best OFET (with highest mobility) are made from single crystals of organic materials. As previous research shows that growing large single crystals of molecular organic materials directly on a substrate is a difficult task, we developed a new approach to the formation of such crystals.

Our work to date has focused on tris-(8-hydroxyquinoline) aluminum (Alq_3), which is commonly used as the emitting layer in organic LEDs. The crystal structures of the Alq_3 α-phase and β-phase [from Brinkmann, et al., J. Am. Chem. Soc., 122, 5147 (2000)] is shown in Figure 46. The widespread use of Alq_3 in OLEDs—including products on the market—results from the amorphous nature of as-deposited films and the high glass transition temperature (T_g=175 °C) of Alq_3. These properties yield efficient and durable devices, yet several studies suggest that device failure can result from crystallization of the Alq_3 film during device operation. Indeed, it has been demonstrated that needle-like crystals form when Alq_3 thin films are thermally annealed at temperatures above T_g. The formation of crystals upon exposure to organic solvent vapors has also been observed. This is likely due to the reduction of T_g by the permeation of solvent molecules into the film, which is a well-known effect—that of plasticization—in the field of polymers.

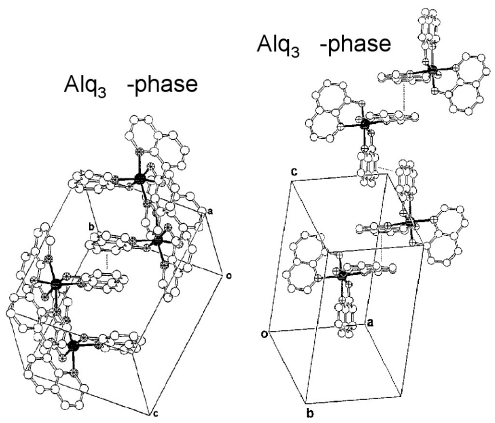

Fig. 46: α and β crystal forms of Alq3. (from Brinkmann, et al., J. Am. Chem. Soc., 122, 5147 (2000).

The crystallization of Alq_3 thin films is detrimental to OLED performance, but it suggests that generating large thin single crystals of organic materials in the plane of the substrate could be possible. A technique that could form such crystals and also direct them along pre-determined substrate directions would be especially useful for OFET use and also for forming single crystals of organic non-linear materials for optoelectronic applications.

We recently demonstrated that nano-patterned substrates can, indeed, be used to direct the flow of solvent-rich thin films of Alq_3 and thereby, generate such oriented needle crystals in the plane of the substrate. The optical micrograph in Figure 47 shows a portion of a nano-patterned substrate with Alq_3 crystals that are predominantly aligned with the underlying nano-grooves.

To generate the crystal needles, Alq_3 is deposited onto nano-patterned Si or SiO_2 substrates by thermal evaporation in vacuum (<10^{-6} Torr). The Alq_3 films are typically 10-20 nm thick and are deposited at rates of 1-3 Å/s (as measured by a quartz crystal thickness monitor) onto room temperature substrates. Prior to Alq_3 deposition, the nano-patterned substrates are cleaned via a sequence of steps involving either sonication in

continued

continued

a solution/solvent or immersion in a boiling solvent. Following the final boiling 2-propanol step, the substrates are dried in a stream of nitrogen and further cleaned by UV-ozone treatment for 5 to 30 minutes. In the case of chemical surface modification, the substrates are placed in a vessel together with a crucible containing n-octadecyltrichlorosilane (OTS). The vessel is evacuated to a pressure of <1 Torr and heated to 120 °C for ~2 hours. Substrates treated in this manner are hydrophobic. Following the evaporation of Alq_3, the substrates are placed in a glass jar together with a beaker of chloroform, and the jar is sealed with a Teflon-lined cap. Exposure of the Alq_3 films to chloroform vapor for times ranging from a few hours to two days results in the formation of elongated Alq_3 crystals that are oriented parallel to the underlying nano-grating. The crystals are characterized by a variety of techniques, including optical microscopy, fluorescence microscopy, Atomic Force Microscopy (AFM), and Scanning Electron Microscopy (SEM).

The nano-patterned substrates are fabricated via interference lithography in the NanoStructures Laboratory (NSL) at MIT. Interference lithography is a maskless lithography in which photoresist is exposed by the optical standing wave generated by the interference of two coherent beams of light. Using the Lloyd's Mirror setup in the NSL, we can generate periodic patterns over square centimeters with feature sizes ranging from 100 to 500 nm. The patterns are transferred to Si or SiO_2 via etching, resulting in surface relief gratings with depths up to 150 nm. After etching, the wafers are cleaned in 5:1:1 H_2O:H_2O_2:NH_4OH at 80 °C for ~10 minutes to remove any remaining anti-reflection coating, SiO_x interlayer, or photoresist. After the wafers are diced into ~cm^2 pieces, these pieces are further cleaned and processed as described above. Figure 48 summarizes all of the fabrication steps, beginning with the nano-lithography, necessary to form oriented crystals of Alq_3. The final step depicted is the evaporation of metal electrodes to enable electrical characterization.

The Alq_3 crystal needles formed in this process vary in size from experiment to experiment, with thicknesses and widths ranging from hundreds of nanometers to a few microns and lengths ranging from a few hundred microns up to one centimeter (the size of the substrate). The needle length can exceed the needle thicknesss and needle width by a factor of 1000 or more. Needle thicknesses exceed the initial Alq_3 amorphous film thickness (typically 10-20 nm) by as much as 200 times. The total volume of a 10 nm thick film on a centimeter square substrate is 10^{-12} m^3. A needle with dimensions 1 μm by 1 μm by 1 cm has a volume of 10^{-14} m^3. Hence, 100 such needles could be formed from the initial thin film, and these needles would be separated by approximately 100 microns. Such a perfect sample has never been produced, but the sizes of the needles formed are consistent with this simple volume analysis. With respect to the nano-pattern dimensions, the needles can be as narrow as one nano-groove or as wide as tens of grooves, and the needle thickness can exceed the groove depth by a factor of 50 or more.

Preliminary electron diffraction data indicates that the needles are single crystals. Other characterization of the needles supports this as well. Figure 49 shows two SEM micrographs of different Alq_3 needles. Micrograph A is a top view of one end of a several micron wide needle, and micrograph B shows the cross section of a smaller needle (the substrate was cleaved in the middle of the needle). Both micrographs show that the needles have distinct crystal facets and tend to be diamond-shaped in cross section. In addition, the fluorescence of the Alq_3 needles is polarized, which is expected if the Alq_3 is crystalline. The graph in Figure 50 plots normalized photoluminescence intensity as a function of polarizer angle, while the fluorescence micrographs shown below the plot correspond to the brightest and dimmest data

continued

continued

points. The discrepancy between the 0° and 180° data points is a result of photobleaching of the needle during the course of the measurements.

The formation of the Alq_3 crystals, such as that in Figure 51, is traced to the exposure of the evaporated thin films to the chloroform vapor. We observe that formed Alq_3 crystals are surrounded by what appear to be amorphous and flowing organic films. The flowing segments are confined by the substrate grooves and are characterized by menisci at both ends in the plane of the substrate and also in cross section. Several of these segments can be seen in the middle of the SEM micrograph of Figure 51 and also surrounding the AFM image inset in the same figure. The menisci of the amorphous segments lend evidence towards a fluid-like state of the Alq_3 thin film in the presence of chloroform. This fluidity can be understood in terms of a plasticization effect, whereby the T_g of a glassy material (typically a polymer) is reduced by the presence of low molecular weight additives. The effect of plasticization on T_g can be roughly estimated by the following semi-empirical equations:

$$T_g \approx \frac{T_{gp}}{1+(X-1)(1-\Phi_p)} \tag{6}$$

$$X \approx \frac{T_{gp}}{T_{gs}} \tag{7}$$

$$T_{gs} \approx \frac{2}{3} T_{ms} \tag{8}$$

These equations are based on free-volume considerations. T_{gp} and T_{gs} are the glass transition temperatures of the pure polymer and pure solvent, respectively, and T_{ms} is the melting temperature of the solvent. Equation 8 is used to estimate T_{gs} based on T_{ms} because T_{gs} has been measured for only a few solvents. Φ_p is the volume fraction of the polymer. Using T_{gp}=175 °C for Alq_3 and T_{ms}=-63 °C for chloroform in the above equations, the predicted effect of chloroform permeation on the T_g of Alq_3 is plotted in Figure 52. As can be seen from the plot, the T_g of Alq_3 is significantly reduced by the presence of the chloroform, dropping to 40 °C when the film is 20% chloroform and falling below room temperature when the film is 25% chloroform by volume. Hence, it is reasonable to suggest that the Alq_3 is able to incorporate enough chloroform to become fluid at room temperature.

It is curious, however, that the amorphous segments, which are the signature of fluid Alq_3, are only observed adjacent to Alq_3 crystals, suggesting that there is a higher concentration of chloroform in the vicinity of the crystals. This could result from a rapid exclusion of chloroform in liquid form as Alq_3 molecules are incorporated into the growing crystal. Another possible explanation is based on the apparent affinity between chloroform and Alq_3, and assumes that the surface of each crystal is coated with a thin layer of fluid, chloroform-rich Alq_3. The large surface area of the crystal relative to that of the crystallite clusters would, therefore, result in a higher concentration of chloroform near the crystal. Indeed, a correlation exists between the size of the crystal and the width of the surrounding region that has experienced flow of chloroform-rich Alq_3. The crystal in Figure 51 is ~300 nm thick and ~600 nm wide, and nano-films are observed in a strip that extends ~2.5 microns to the right of the crystal (similarly on the other side of the crystal). In comparison, for a smaller needle that is ~130 nm thick and ~400 nm wide, the width of the strip containing nano-films is only one to two grating periods (300-600 nm). Therefore, as a crystal grows, an increasing concentration of chloroform at the crystal surface (due to increasing surface area) causes the surrounding region of flowing Alq_3 to widen. In some cases, extended nano-films (exceeding several microns in length) are present in the grooves immediately adjacent to an Alq_3 crystal. This implies that the crystal was in a very active stage of growth—

continued

continued

having a plentiful supply of fluid Alq_3 close by—when the vapor treatment was terminated. In fact, the crystals likely grow up out of the Alq_3 that flows in the nano-grooves as evidenced by the nano-films that are protruding out from underneath the crystal tip in the AFM micrograph of Figure 51.

Although the individual amorphous segments and crystallite clusters are too small to be resolved by optical microscopy, the regions of the substrate with clusters can be distinguished from amorphous flow regions in optical micrographs. For example, the darker, speckled region of the substrate on the left in Figure 47 is a region with crystallite clusters. The rest of the substrate surrounding the crystals has experienced flow of chloroform-rich Alq_3.

What is astonishing about the flow regions of Figure 47 is the extent to which they extend beyond the ends of the crystals in the direction parallel to the underlying nano-grooves. This sheds light on the critical role played by the substrate nano-pattern in the formation of the Alq_3 crystals. What has been emphasized up to this point is that the incorporation of enough (~25% by volume) chloroform can cause Alq_3 to become fluid at room temperature, but this seems to happen only near crystals. As was mentioned before, this suggests that there is extra chloroform associated with the crystals, possibly due to a thin fluid layer of chloroform-rich Alq_3 on the crystal surface. It is also likely that chloroform is excluded as Alq_3 molecules are incorporated into a crystal. Since the atmosphere in the vapor treatment jar is already saturated with chloroform vapor, it is reasonable to assume that the excluded chloroform will remain on the substrate as a liquid. The chloroform can then flow on the substrate, but due to capillary effects, it prefers to flow down the nano-grooves of the patterned substrate. As it flows down the grooves, it encounters and permeates Alq_3, reducing its T_g, and allowing it to flow down the grooves as well. It is in this way that the nano-grooves aid the transport of Alq_3 to the forming crystals, and this also explains the elongation of the flow regions parallel to the nano-grooves.

A transport ratio can also be calculated from substrates with much more extensive Alq_3 flow and crystal formation, such as the substrate shown in Figure 47. The distance traveled by Alq_3 perpendicular to the nano-grooves can be ascertained by the gap between the (speckled) crystallite cluster region on the left side of the micrograph and the leftmost crystal. This gap is ~200 microns wide. In contrast, the typical distance parallel to the nano-grooves separating the cross needles from the oriented needles is ~2 mm, indicating that the Alq_3 was able to flow at least 1 mm down the nano-grooves to reach a crystal. The calculated transport ratio in this case is only 1:5, but this is likely a conservative estimate since the flow is so widespread and may even have been limited by the size of the substrate. The large size of the cross crystals can be understood in terms of the large number of nano-grooves intersected by these crystals relative to the number of grooves that directly feed the oriented crystals.

While the proposed mechanism for crystal growth via capillary flow of chloroform-rich Alq_3 down substrate nano-grooves in the vicinity of pre-existing crystals seems well-supported, the question remains as to how the crystals are formed initially. It is possible that crystallites present in the as-deposited films seed the growth, or that crystallite clusters (formed during exposure to chloroform vapor) of a certain size can act as a seed. Whatever the case may be, it seems that the requirement for crystal formation is a large enough concentration of chloroform to initiate significant flow of Alq_3. Although the exact mechanism for the nucleation of the crystals is not fully understood at this time, the ease of formation of crystals of such large dimensions in the plane of a substrate is a technological breakthrough in the field of organic electronics.

continued

continued

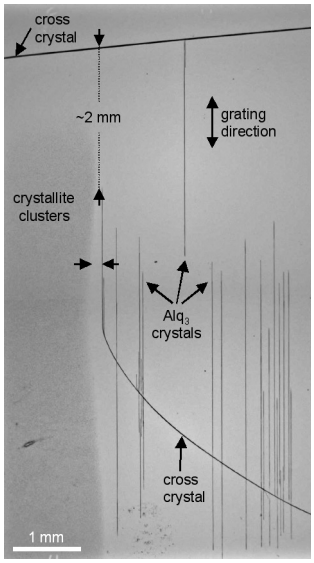

Fig. 47: Macroscopic Alq_3 crystals on a nanopatterned substrate.

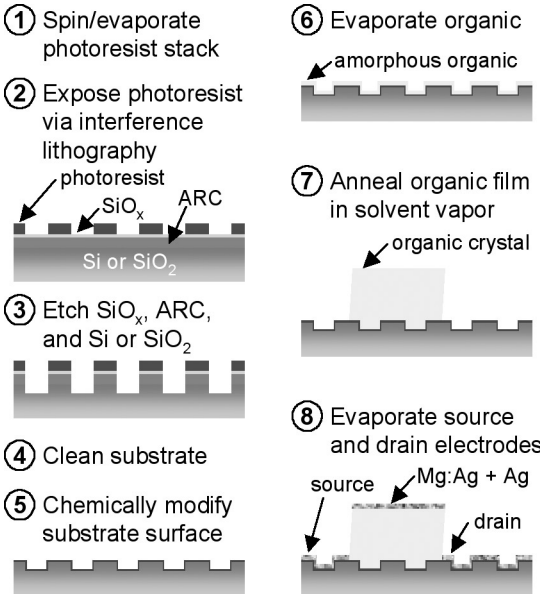

Fig. 48: Fabrication steps, beginning with the nano-lithography, necessary to form oriented crystals of Alq_3.

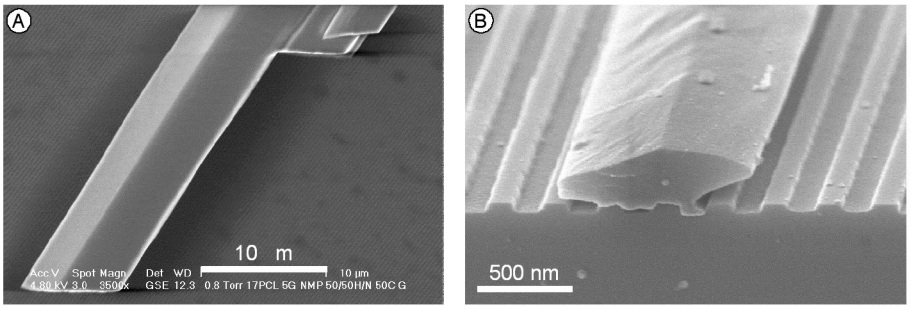

Fig. 49: SEM micrograph of two Alq_3 crystals. (A) is a top view of one end of a several micron wide needle, and (B) shows the cross section of a smaller needle (the substrate was cleaved in the middle of the needle).

continued

continued

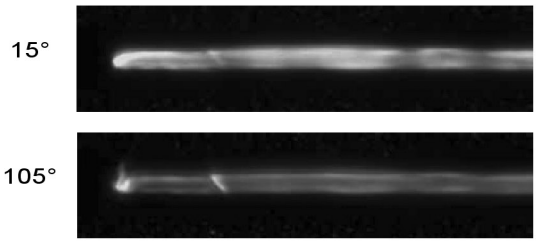

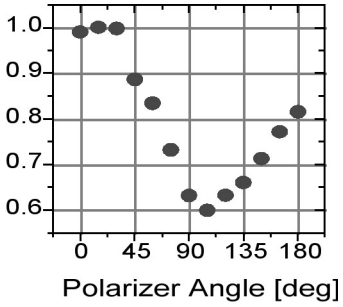

Fig. 50: (left) Polarized fluorescence micrographs (UV excitation at 449 nm) for two orthogonal polarizer angles. (right) The graph plots the normalized photoluminescence intensity as a function of polarizer angle.

Fig. 51: (left) SEM and (right) AFM micrograph of a Alq_3 crystal and vicinity.

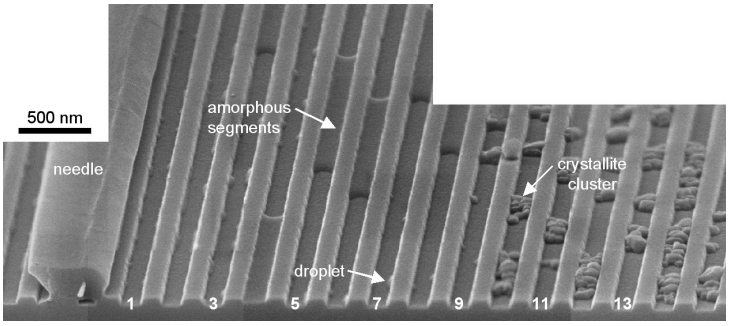

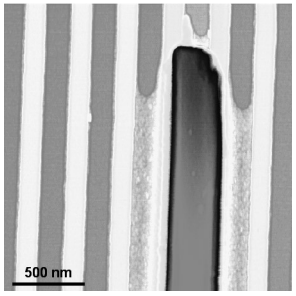

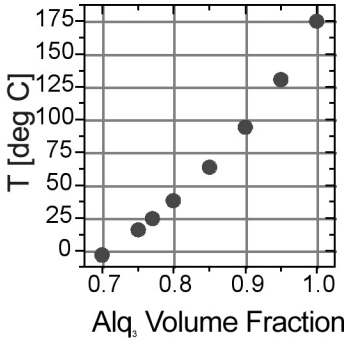

Fig. 52: Change in the glass transition temperature of Alq_3 upon incorporation of chloroform.

Strain-Tunable Photonic Band Gap Microcavity Waveguides at 1.55 μm

Personnel
C. W. Wong, M. Qi, P. Rakich, S. G. Johnson and Y. B. Jeon (G. Barbastathis, S-G. Kim and H. I. Smith)

Sponsorship
MIT Microphotonics Center

We have designed and fabricated tunable photonic-bandgap microcavities in optical waveguides, with strain modulation via thin-film piezoelectric actuators on deformable membranes. Cavity resonance tunability, with nanometer lattice control, is designed through perturbation on Finite-Difference Time-Domain FDTD computations. Device fabrication integrates X-ray nanolithography, piezoelectric micro-actuators and bulk micromachining.

Photonic-bandgap microcavities in optical waveguides have demonstrated cavity resonances at wavelengths near the 1.55 μm band, quality factors on the order of 300, and modal volume at 0.055 μm^3 in high-index contrast Si/SiO_2 waveguides and GaAs air-bridge waveguides. Applications include zero-threshold microlasers, filters, and signal routers. For tunability in Si microphotonic platforms, thermal actuation is often utilized. Compared to thermo-optics, strain-tuning via thin-film piezoelectric micro-actuators provides a significantly faster response, lower power consumption, and better localization of tunability. This level of integration permits dynamic reconfiguration of the cavity resonance and band-edges, fine-tuning for fabrication mismatches, and active compensation of device arrays to external disturbances.

The conceptual design is illustrated in Figure 53. The Si microcavity waveguide is located on a deformable double-anchored SiO_2/Si membrane. The thin-film piezoelectric actuators provide sufficient driving force, under 5 V actuation, for the sub-nanometer strain control of the geometric lattice in the microcavity. Comparative designs of the double-anchored membrane have been demonstrated for analog tunable diffractive gratings. Experimental effects of static strain on coupled vertical microcavity resonators and theoretical designs for shear-modulated 2D photonic crystals on bulk piezoelectric substrates have also been reported.

We employ first-order perturbation theory to obtain a semi-analytical result for the strain-induced shift in the cavity resonance; such methods ease the study of small modulations such as the 0.3% strain considered here. First, a closed-form solution for the hole boundary displacements is derived following classical mechanics. The material boundary displacements are then numerically meshed and employed in a perturbation-theory formulation, which involves surface integrals of the unperturbed fields (obtained by FDTD simulation) over the perturbed material boundaries. The result predicts a 0.8% shift in resonant wavelength (12.7 nm in the C-band) for a 0.3% mechanical strain from a 3D computation. This is illustrated in Figure 54a. While a 2D computation suggests similar final results in the resonant shift, the 3D computation highlights differences from the individual contributions – hole ellipticity, defect cavity length, and hole diameters – in the strain perturbation. Other effects such as photoelasticity and waveguide out-of-plane bending were found to be secondary.

For resonance wavelength at 1.55 μm, the minimum feature size, located between the waveguide edges and the hole edges, is 130 nm. X-ray lithography is employed with a Cu_L source at 1.3 nm to transfer the pattern from the mask to a PMMA resist. The mask is a thin SiN_x membrane with 200 nm Au patterned with e-beam lithography. The resist image is then transferred to 50 nm of Cr, via lift-off, and etched into a 212 nm single-crystal Si layer to form our waveguide. The microfabricated piezoelectric film has an excellent dielectric constant of 1200 and a d_{31} coefficient of ~ -100 pC/N. A fiber lens assembly is used to couple a 1.430 μm to 1.610 μm tunable laser diode source, with TE polarization and lock-in amplification, into the prepared input/output waveguide facets. For a static microcavity waveguide, resonance is detected at 1555.4 nm with a Q of 159, as shown in Figure 54b. Experimental measurements of the tunable cavity resonance, band-edges, and other cavity responses are currently underway.

continued

continued

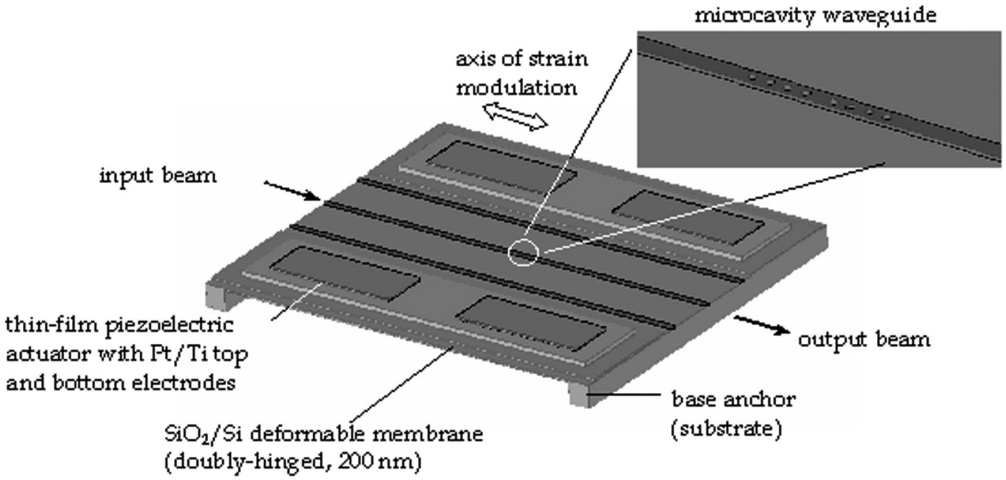

Fig. 53: Device schematic of the tunable photonic-bandgap microcavity waveguide, with strain modulation via thin-film piezoelectric actuators on the deformable membrane.

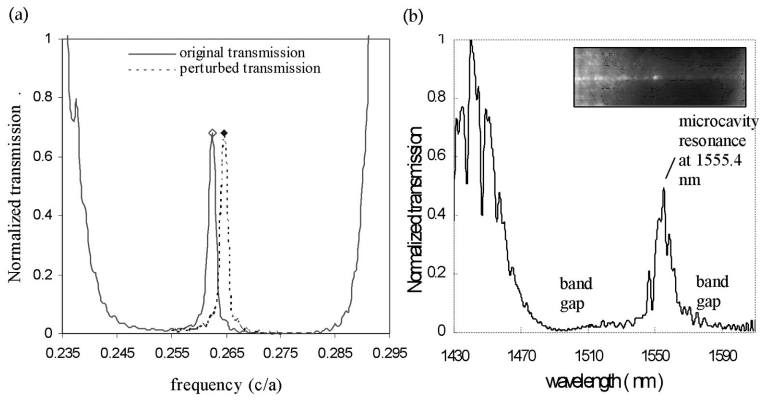

Fig. 54: (a) Computed transmission shift through perturbation theory in the photonic band gap, (b) Measured static microcavity resonance with Q of 159. Inset: top view of microcavity waveguide in transmission.

Nanopelleting of Carbon Nanotubes

Personnel

T. El-Aguizy, Y. Jeon, and J.-H. Jeong (S.-G. Kim)

Sponsorship

Deshpande Center Ignition Grant

A novel method of decoupling the growth and the assembly of Carbon NanoTubes (CNT) has been invented. The objective of this project is to make a long range ordered CNTs on a large area, which has not been possible with the existing nanotube growing processes. Nanopelleting is the technology to transform carbon nanotubes into the handleable and manufacturable form with which the existing micro-scale manufacturing processes can be utilized, such as fluidic self assembly or MEMS manupulators. To achieve this, small blocks (nanopellets) of material encapsulating CNTs with known length and alignment are going to be made (See Figure 55). The CVD growth of individual free-standing nanotubes in arrays of Silicon trenches followed by the encapsulation and CMP will form nanotube-embedded nanopellets. Various self-assembly methods can then be utilized to locate the individual nanopellets at points of use. The nanopelleting material must allow for selective release from the substrate material as well as selective removal of the nanopellet material without affecting the CNTs.

Fabrication of the silicon trenches can be achieved utilizing anisotropic wet etching of (100) wafers to allow for well-defined sloping sidewalls that facilitate self-assembly. The desired geometry and periodicity can be achieved by tailoring the mask pattern and etch parameters to achieve the desired geometry and periodicity in the resulting trenches. Nickel nanodots with diameters of several microns are currently used as the catalyst patches in CNT growth. Interference lithography and X-ray lithography are well suited for patterning periodic patterns in the sub-micron regime, and we investigate their potential for patterning sub-micron (200nm) nanodots aligned with the etched trench patterns.

Several methods exist for growing single or multi-walled CNTs, including arc discharge and CVD methods. Plasma Enhanced (PE) CVD methods provide a reliable, low-cost option for growing well-ordered, aligned CNT over large areas. We have established a collaboration with Z.F. Ren of Boston College to utilize their PE-CVD device for growth of aligned CNTs. Advantages of this approach include: the lower temperatures required for nanotube formation, the flexibility in the range of catalytic materials used, and the inherent e-field that assists in growth of aligned CNTs.

We are investigating various materials for filling the nanopellets to satisfy the functional requirements (See Figure 56). Spin-coated M-Bond epoxy is found to allow selective release of the nanopellets from a silicon substrate utilizing xenon di-fluoride (XeF_2) as well as the selective removal of the M-Bond without attacking the CNT utilizing oxygen plasma etching. We are also investigating the possibility for utilizing conventional chemical-mechanical planarization methods to eliminate any excess filler material, leaving independent nanopellets with well-defined geometry encapsulating aligned CNTs with well-defined lengths and diameters.

continued

continued

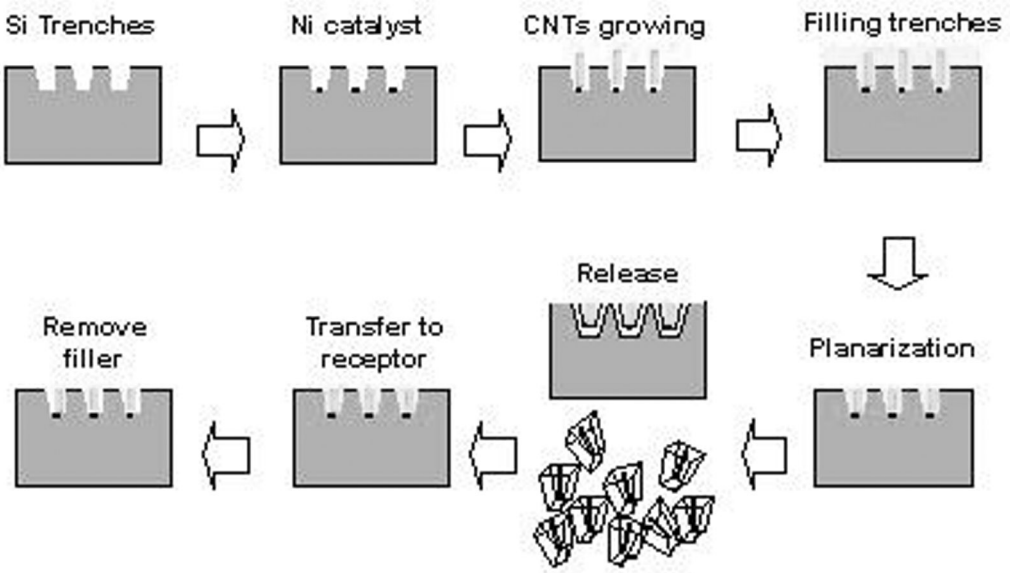

Fig 55: *Nanopelleting of CNTs*

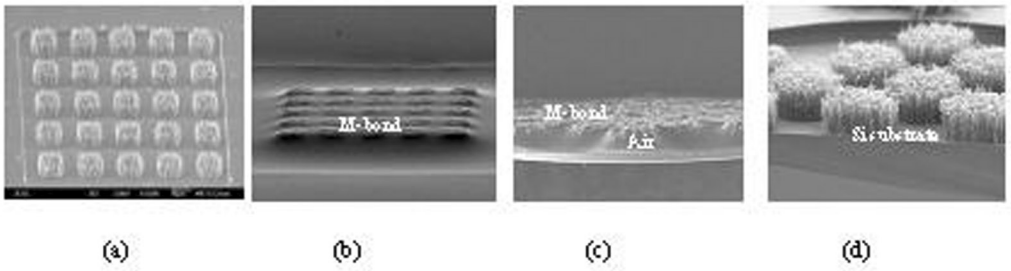

Fig. 56: SEM images of the CNTs (a) Grown CNTs, (b) Filled with M-bond, (c) Released M-bond pellet by XeF_2 (not planarized) and (d) CNTs after filler removal by O_2 plasma (not planarized)

Nanofabricated Reflection Gratings

Personnel

J. Carter, C.-H. Chang, R.C. Fleming, R. Heilmann, and E. Murphy
(M.L. Schattenburg, C.R. Canizares and H.I. Smith)

Sponsorship

NASA and Chromaplex Corp.

Grazing-incidence X-ray reflection gratings are an important component of advanced high-resolution spectrometers and other X-ray optics. These have traditionally been fabricated by diamond scribing with a ruling engine or by interference lithography followed by ion etching. These methods result in gratings which suffer from a number of deficiencies, including high surface roughness and poor groove profile control, leading to poor diffraction efficiency and large amounts of scattered light.

We are developing improved methods for fabricating blazed X-ray reflection gratings which utilize special (111) silicon wafers, cut ~1 degree off the (111) plane. Silicon anisotropic etching solutions, such as potassium hydroxide (KOH), etch the (111) planes very slow compared to other crystallographic directions, resulting in the desired super-smooth blaze surface. Previous work used similar off-cut (111) silicon substrates to fabricate blazed diffraction gratings, but utilized a second KOH etch step that compromised the grating facet flatness and proved unsuitable for small grazing-angle X-ray diffraction.

Gratings are patterned using interference lithography with the l=351.1 nm wavelength, and transferred into the substrate using tri-level resist processing, Reactive-Ion Etching (RIE), and silicon-nitride masking during the KOH etch. The narrow (~100 nm) ridge of silicon which supports the nitride mask is removed using a novel chromium lift-off step followed by a CF_4 RIE. The result is extremely-smooth sawtooth patterns, which, after applying a thin evaporative coating of Cr/Au, are suitable for X-ray reflection (See Figure 57).

We have recently begun a new effort to replicate sawtooth gratings using nano-imprint lithography with a UV-curable polymer (See Figure 58). If successful, this new method promises to significantly reduce the cost of grating fabrication.

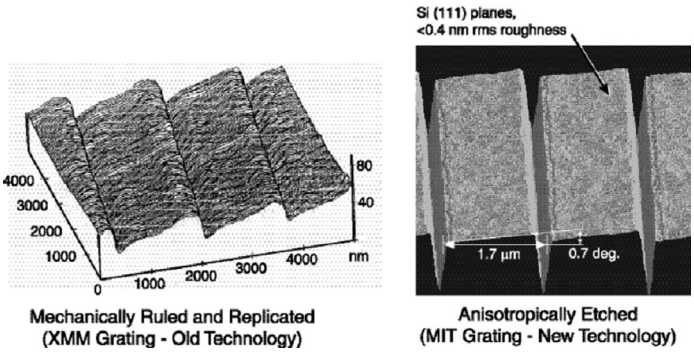

*Fig. 57: (a) An AFM image of a traditional mechanically-ruled and replicated X-ray reflection grating (Bixler et al., Proc. SPIE **1549**, 420-428 [1991]). Note the rough, wavy grating surfaces that lead to poor diffraction performance. (b) An AFM image of a blazed X-ray reflection grating fabricated by anisotropic etching of special off-cut (111) silicon wafers. Note the improvement of grating surface flatness and smoothness, leading to significantly improved performance.*

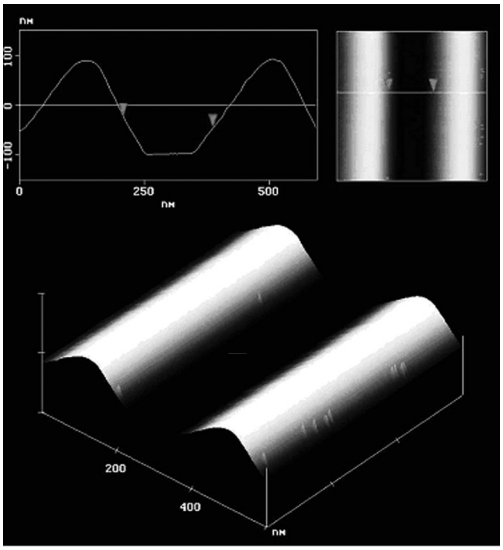

Fig. 58: AFM image of nano-imprinted grating. Profile is far from ideal at this stage.

Transmission Gratings for X-ray and Atom-Beam Spectroscopy and Interferometry

Personnel

J.M. Carter, T.A. Savas, and E. Murphy (H.I. Smith and M.L. Schattenburg)

Sponsorship

X-OPT, Inc.

Transmission gratings with periods of 100 to 1000 nm are widely used in applications such as X-ray, vacuum-ultraviolet, and atom-beam spectroscopy and interferometry. Over 30 laboratories around the world depend on MIT-supplied gratings in their work. For X-ray and VUV spectroscopy, gratings are made of gold and have periods of 100 to 1000 nm, and thicknesses ranging from 100 to 1000 nm. The gratings are most commonly used for spectroscopy of the X-ray emission from high-temperature plasmas. Transmission gratings are supported on thin (1 micron) polyimide membranes, or made self supporting ("free standing") by the addition of crossing struts (mesh). (For short X-ray wavelengths, membrane support is desired, while for the long wavelengths, a mesh support is preferred in order to increase efficiency.) Fabrication is performed by interference lithography combined with reactive-ion etching and electroplating. Progress in this area tends to focus on improving the yield and flexibility of the fabrication procedures.

Another application is the diffraction of neutral-atom and molecular beams by mesh-supported gratings. Lithographic and etching procedures have been developed for fabricationg free-standing gratings and grids in thin silicon nitride (SiNx) membranes supported in a Si frame. Figure 59 shows a free-standing 100 nm-period grating in 100 nm-thick silicon nitride. Figure 60 shows a 100 nm-period grid in a 100 nm-thick SiNx membrane. Such a grid is used in experiments as a "molecular sieve."

We have established a collaboration with the Max-Planck Institute in Göttingen, Germany, in which they utilize our gratings of 100 nm period in diffraction experiments using atomic, molecular, and helium-cluster beams. As shown in Figure 61, the diffraction of atomic and molecular beams reveals striking deviations from Kirchhoff's optical diffraction theory. The analysis of the diffraction intensities enabled a quantitative determination of the attractive van der Waals interaction between the silicon nitride surface and various atomic and molecular species, including He, Ne, Ar, Kr, He*, Ne*, D_2, and CH_3F. The diffraction of cluster beams by a transmission grating has been established as a unique technique for the non-destructive mass selection and detection of small and weakly bound van der Waals clusters. Recently, the Göttingen group discovered bound states in mixed-isotope helium clusters, e.g. $^3He^4He_2$, $^3He^4He_3$, etc., by diffraction from one of our 100-nm-period gratings as shown in Figure 62. In addition, they employed the grating to measure the bond length of the helium dimer, $^4He_2$, which is assumed to be the weakest molecular bond. Future experiments based on the transmission gratings include the study of cluster formation dynamics and the search for the Efimov effect in the helium trimer.

Data obtained by helium-atom-beam diffraction at large incident angles showed Lyman ghosts in the spectrum. This data led to the development of new fabrication techniques to improve the quality of the free-standing gratings in silicon nitride. Diffraction spectra from gratings made with the improved process show no Lyman ghosts, illustrating the important synergy between applications and nanofabrication.

Successful diffraction experiments with beams of buckyballs (C60) have been carried out with our 100 nm-period, free-standing SiNx gratings by Dr. Markus Arndt of the University of Vienna. In addition, our 100 nm-period, free-standing SiNx gratings can be lightly coated with metal. Prof. Herman Batelaan of the University of Nebraska-Lincoln has used such gratings in highly-successful diffraction experiments with beams of 500 eV electrons.

Our 100 nm-period free-standing SiNx gratings are also used for atom interferometry by two groups: those of Prof. Alexander Cronin of the University of Arizona

continued

continued

and Prof. Bruce Doak of the State University of Arizona. Cronin's group interferes neutral beams of sodium atoms, while Doak's group interferes helium beams (performed at the Max Planck Institute in Göttingen, Germany in collaboration with P. Toennies).

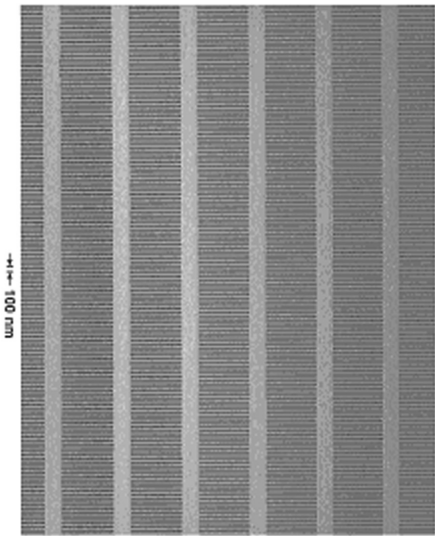

Fig. 59: Scanning electron micrograph of a free-standing 100 nm-period grating (50 nm-wide bars) in a silicon nitride membrane of area 500 microns by 5 mm.

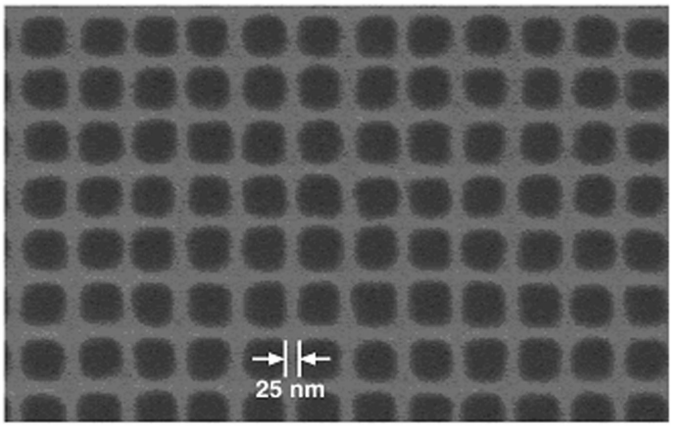

Fig. 60: Scanning electron micrograph of a free-standing 100 nm period grid in a silicon nitride membrane of area 500 micron by 5 mm. Such grids are used in experiments to separate out Helium trimers from other clusters.

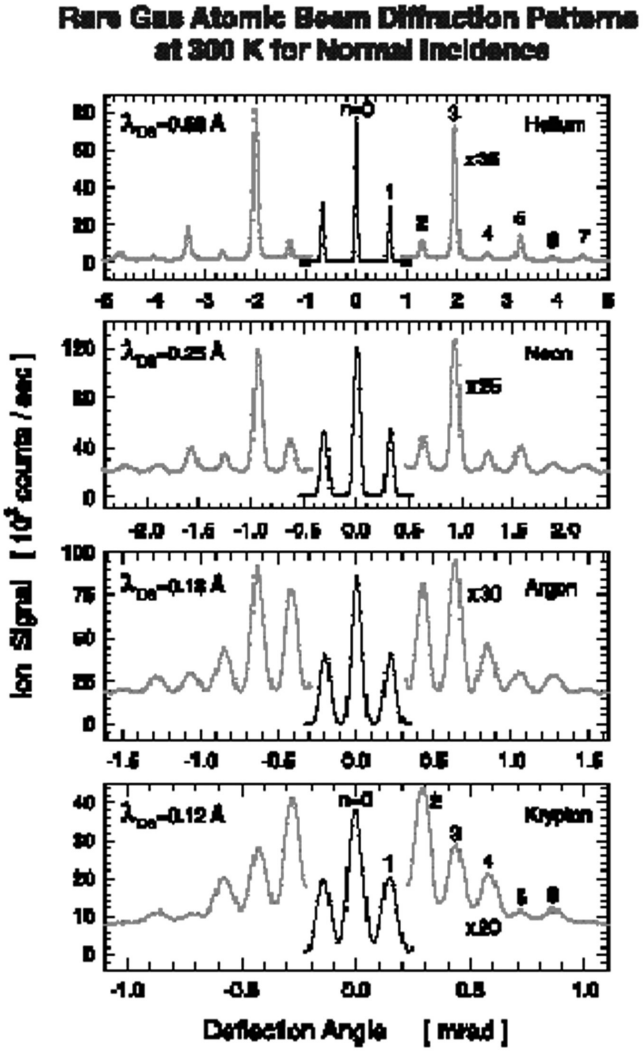

Fig. 61: Rare-gas atom-beam diffraction patterns. These results were obtained by Wieland Schöllkopf and Peter Toennies at the Max-Planck Institute in Göttingen, Germany, using a free-standing, 100nm-period grating

continued

continued

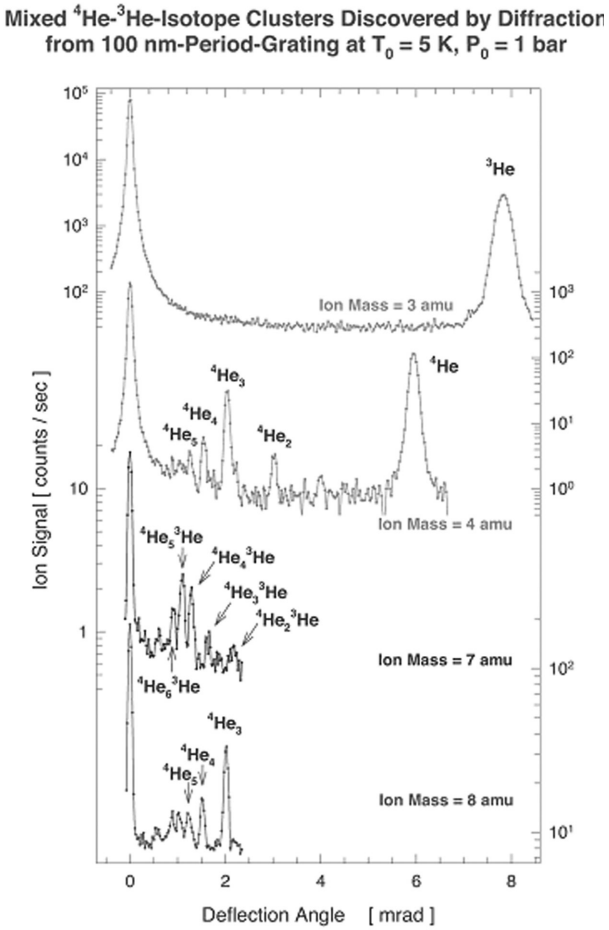

Fig. 62: Non-destructive mass separation of small mixed-isotope helium clusters. These results were obtained by Peter Toennies, et al, at the Max-Planck Institute in Goettingen, Germany, using free-standing, 100 nm-period gratings made in the NSL at MIT.

X-Ray Foil Optics Shaping Technology

Personnel

M. Akilian, C. Forest, Dr. R. Heilmann, and Y. Sun
(C.R. Canizares, G.R. Ricker and M.L. Schattenburg)

Sponsorship

NASA and QED, Inc.

Future X-ray astronomy missions will require orders-of-magnitude improvement in collecting area and resolution. Thin-foil optics are attractive candidates for X-ray telescopes because of the tremendous weight and cost savings which can be achieved compared to traditional monolithic optics. However, substantial improvement in our ability to shape foils to high accuracy is required. In this research program we are developing technology for high-volume shaping of thin (~0.5 mm) glass and silicon substrates, including both reflective and diffractive components.

Over the last several years we have developed methods for thermally shaping glass sheets. This process involves heating the sheet in a furnace until it begins to slump, conforming to quartz or silicon mandrels that have been lithographically patterned with thousands of pins. The pins reduce the surface area of the mandrel to minimize sticking and mitigate the effects of dust particles. We are also developing an alternative slumping method based on air bearings.

We are also developing a complementary shaping process called block lapping. This novel process involves the bonding of foils to rigid polishing blocks, while in their relaxed state, using special UV-cured epoxies and thermoplastics. The bonded foils are then mechanically polished into the desired shape.

A third method involves a process called Magneto-Rheologic Fluid polishing (MRF) to deterministically shape the surface of the substrate. A magnetic polishing compound is entrained onto a spinning sphere that is scanned over the substrate. A magnetic field stiffens the fluid in a confined area generating high shear polishing forces. This method requires an accurate surface error map as input to the MRF shaping machine.

A critical component of this research is accurate surface metrology of thin foils. We are developing a variety

continued

continued

Nano-Accurate Assembly Technology for X-Ray Foil Optics

Personnel
M. Akilian, C. Chen, C. Forest, R. Heilmann, and Y. Sun (C.R. Canizares, A. Slocum, G.R. Ricker, and M.L. Schattenburg)

Sponsorship
NASA

of Hartmann and Shack-Hartmann surface metrology tools for this purpose, and special fixturing that holds the sheets during metrology, while minimizing holding torques and gravity distortions.

Our short-term goal is to develop foil shaping technology with sub-500 nm accuracy. This will enable a number of important NASA missions such as *Constellation X*. Our long term goal is to realize sub-20 nm shaping accuracy, which will enable diffraction-limited X-ray imaging with resolution improved ~1000X more than today's telescopes.

Future X-ray astronomy missions will require orders of magnitude improvement in collecting area and resolution. Foils optics are attractive candidates for X-ray telescopes because of the tremendous weight and cost savings which can be achieved compared to traditional monolithic optics. However, substantial improvements in our ability to assemble foils with high accuracy are required. In this research program, we are developing microstructures to assemble foil optics, including both reflective and diffractive components.

Plasma micromachining is used to lithographically fabricate silicon "micro-combs" designed to guide and register silicon and glass foils into precise three-dimensional shapes with sub-micron accuracy. Thousands of ~500 μm-thick foils are typically required in an X-ray telescope, each shaped and assembled to form the precise curves or flats that focus X-rays by grazing-incidence reflection. Figure 63 shows SEM images of two types of micro-combs under development.

A prototype flight mirror structure based on these principles has been built and tested. Test results show that glass sheets are assembled to a repeatability of ~0.3 micron, corresponding to an angle error of <1 arc-second. This accuracy exceeds previous foil assembly methods by a factor of ~100. Our microstructure technology is being supported by NASA as the baseline technology for assembling foil optics in the *Constellation X* telescope.

Recent effort seeks to improve the accuracy of the micro-combs from the current level of ~200 nm to under 100 nm. With further progress it may be possible to achieve diffraction-limited X-ray imaging, which can potentially improve the accuracy of telescopes by over 1000X.

continued

continued

Functional 3D Nanostructures Achieved via Folding of 2D Membranes

Personnel

S.M. Jurga and C.H. Hidrovo-Chavez
(G. Barbastathis and H.I. Smith)

Sponsorship

NSF

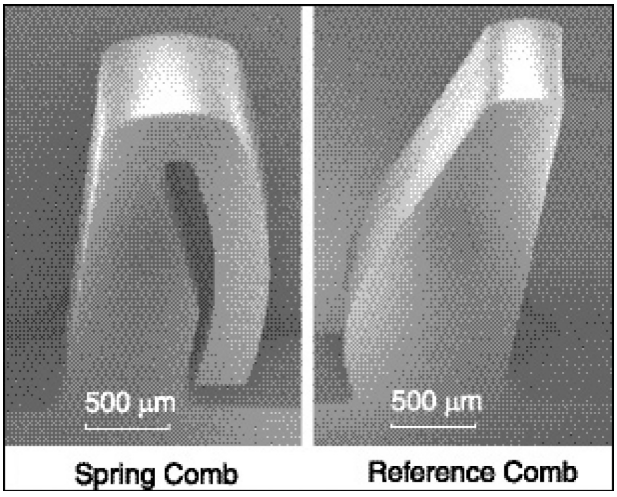

Fig. 63: Electron micrographs of silicon micro-combs. Teeth are ~500 µm wide. a) Spring comb. b) Reference comb.

Functional Three-Dimensional (3D) nanostructures are of interest in numerous technological domains. The 3rd dimension promises to extend micro processors and memories beyond "the end of Moore's law," *i.e.* when feature sizes of planar electronics reach their minimum practical limit. In applications other than electronics, the need to conquer the 3rd dimension is even more urgent; examples include optical elements that integrate sensing and processing for defense or commercial applications, miniature reactors for chemical and biochemical analysis, drug delivery by miniaturized microfluidic implants, micromechanical and nanomechanical energy storage elements, and environmental monitoring and industrial quality control applications. However, 3D fabrication is not well understood and developed. Our CMSE seed grant research is aimed at 1) developing a specific method for 3D fabrication and assembly, which we refer to as "membrane folding.," and 2) conducting a case study in three-dimensional diffractive optical elements.

For a three dimensional technology to be successful and widely applicable to the worlds of solid-state electronics, MEMS, and nanomanufacturing, it must satisfy the functional requirement of sufficient connectivity between the micro and nano devices that compose the system (i.e. the transistors and capacitors of a microchip). Additionally, a winning technology must avoid fighting against the momentum of an existing industry with established tool-sets and large capital investments; a new 3D technology must be easily integrated and compatible with current methods of fabrication that remain planar in nature (i.e. photolithography, plasma etching and deposition are all 2D).

Our approach is a two step process designed to satisfy the following functional requirements: (a) integration of dimensional scales from the nano to the micro and beyond; (b) maximum utilization of existing fabrication tools; and (c) flexibility in achieving a large number

continued

continued

of possible 3D configurations with minimum cost and maximum repeatability and yield. In the first step, all devices are fabricated on a planar substrate just as they are in today's semiconductor industry. In the second step, the planar substrate is folded into a 3D structure as depicted in Figure 64. Designated compliant zones act as hinges between stiffer regions that contain micro and nano devices. By virtue of compliant circuitry that spans the hinge areas, full 2D connectivity is preserved across the entire length after folding. This is important for electronics as well as communication in MEMS sensors and actuators and integrated nano devices. Connectivity may also be achieved in the vertical, 3rd direction by designing vertical connections to be formed when the planar folds reach predetermined locations during folding.

At present, our study aims to build 3D Diffractive-Optical Elements (3D-DOEs) as a case study in the technology development for folded-membrane devices. 3D-DOEs promise better performance in terms of efficiency and angular selectivity than traditional 2D diffractive-optical elements. Spacing multiple diffractive gratings or Ffresnel zone plates (perhaps as many as 50) vertically above one another establishes a matched filter with very high efficiency. Although such a 3-D structure could be fabricated one layer at a time, the folded-membrane approach should be far more cost effective. Also, the folded membrane approach may enable tuning of the diffractive optical systems, for example, by electrically varying the spacing of the stack.

In our preliminary work, we have demonstrated a single 180 degree fold in a silicon-based device with magnetic-actuation-effectinginduced folding (See Figure 65). The gold hinges are plastically deformed so that the folded membrane remains near 180 degrees. Electron beam evaporated gold was chosen for the compliant hinges due to its high ductility and comparatively small spring back angle. The hinges also complete a current loop around the perimeter of the membrane. By placing the device in a magnetic field and controlling the magnitude of current in this loop, a Lorentz force is generated that rotates the flap about its hinges. The Lorentz force is highly controllable and thus allows extensive experimental characterization of the mechanics of folding in our device. In the future, we will also explore other means of actuation such as stress and chemically-induced folding. Some of these alternatives are more attractive than the magnetic method from the point of view of alignment and flexibility in 3D assembly schemes. is an ideal means of actuation for the first round of prototypes because it is a highly controllable force that allows for good experimental analysis of the mechanics of folding.

The first 3D diffractive device is displayed in its unfolded state, still attached to the substrate in Figure 66. Electrostatic combdrives tune the period of the binary grating, which changes the angle of the diffracted orders. The Fresnel zone plate (essentially a diffractive lens) will be folded over and aligned to the grating as a demonstration of compound diffractive optics in 3D. Future work will focus on the final alignment and latching of the folds in addition to new actuation methods for folding that could be categorized as templated-self-assembly. Work in implementing multiple folds and studying the behavior of multiple folds is also underway. These steps are the early formative building blocks for establishing a multi-use platform. 3D assembly through folding lends itself to a broader goal such as combining discrete devices of varied functionality (optics, electronics, microfluidics, etc) into one cohesive, self-contained system capable of multiple tasks such as advanced sensing and response.

continued

continued

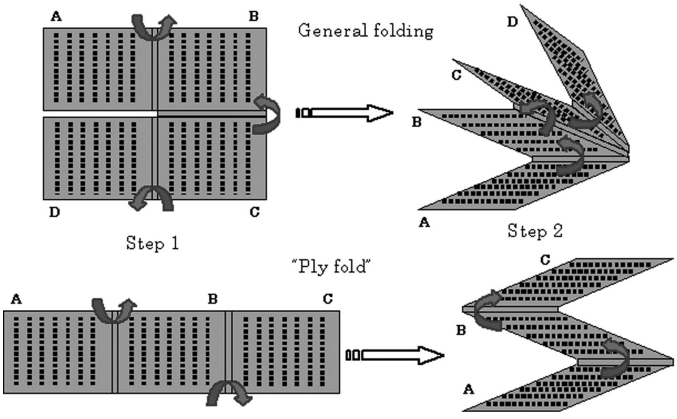

Fig. 64: Examples of how 3D structures can be obtained by folding pre-fabricated thin 2D membranes in a two step process. Black dots

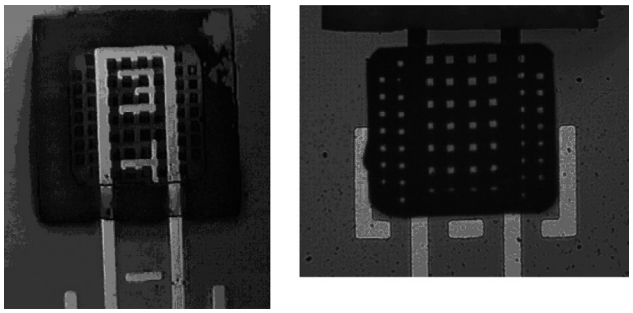

denote surface features nanofabricated on the membrane surface. Fig. 65: Membrane flap before folding (left) and after folding to 180 degrees (right). Note the alignment tolerance achieved in folding. (Alignment fiducials are 50mm wide).

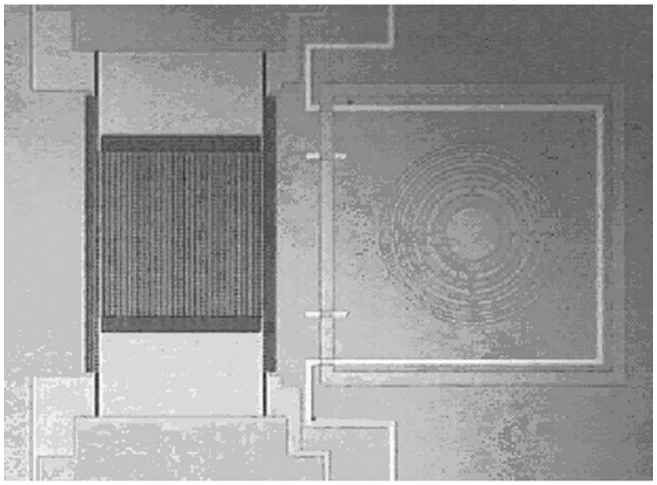

Fig. 66: Top view of tunmable grating (left) and static Fresnel zone plate (right) before release from substrate and before folding.

Integration of Nanowires Embedded in Anodic Alumina Templates with a Large Silicon Substrate

Personnel

O. Rabin, P. R. Herz, Y.-M. Lin, and S. B. Cronin (A. I. Akinwande and M. S. Dresselhaus)

Sponsorship

Navy, ONR MURI, DARPA, and ONR

More and more new miniature devices include nanowire components, exploiting the unique properties of these nanostructures for optical, electronic, and sensing applications. Nanowires can show enhanced quantum and surface effects, while still providing a guiding path for electrons or photons to transmit electrical or optical signals, respectively. In this context, we have developed a non-lithographic process to fabricate arrays of metallic and semimetallic nanowires, aligned perpendicular to the surface of a silicon wafer. The process takes advantage of the self-assembly of an array of pores during the anodization (electrochemical oxidation) of aluminum to Porous Anodic Alumina (PAA). The PAA is grown on top of a silicon wafer coated by a conductive layer (Ti or Ti/Pt) which serves both as an adhesion layer to the wafer, and as an anodization barrier to protect the wafer. The PAA is used as a template for the growth of nanowires by filling its pores with the chosen nanowire material. This can be done electrochemically, using the conductive layer on the wafer as a cathode for the electrodeposition of metallic nanowires into the pores of the PAA. The geometrical parameters of the PAA (thickness and pore diameter, controlled by the anodization conditions) dictate the shape of the wire, while the electrodeposition process dictates its composition profile. In addition to the mechanical advantages of mounting the nanowire arrays on silicon wafers, this process greatly facilitates the establishment of electrical contact to both ends of millions of nanowires, which we utilized to measure the transport properties of these arrays (See Figure 67). The integration of the array on a silicon wafer offers a convenient way to construct nanowire-based devices, such as field emitters, thermoelectric coolers, and photo-diodes.

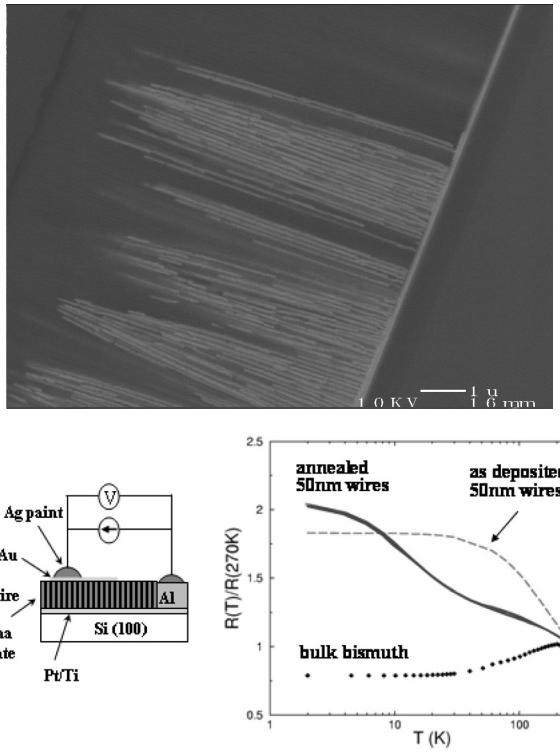

Fig. 67: Cross-section SEM micrograph of bismuth nanowire arrays grown on a Pt-coated silicon wafer. Scheme of 2-point resistance measurement setup. Resistance versus temperature characteristics of electrodeposited bismuth nanowire arrays.